Stefan Diebald

Theory of Electrons in Crystalline Materials, Investigated by Doppler Spectroscopy

DIPLOMARBEIT

zur Erlangung des akademischen Grades Diplom-Ingenieur
in der Studienrichtung Technische Physik

Graz University of Technology

Betreuer:
Ao.Univ.-Prof. Dipl.-Ing. Dr.techn. Heinrich Sormann
Institut für Theoretische Physik - Computational Physics
Graz, Oktober 2010

EIDESSTATTLICHE ERKLÄRUNG

Ich erkläre an Eides statt, dass ich die vorliegende Arbeit selbstständig verfasst, andere als die angegebenen Quellen/Hilfsmittel nicht benutzt, und die den benutzten Quellen wörtlich und inhaltlich entnommenen Stellen als solche kenntlich gemacht habe.

Graz, am 25. Oktober 2010

STATUTORY DECLARATION

I declare that I have authored this thesis independently, that I have not used other than the declared sources / resources, and that I have explicitly marked all material which has been quoted either literally or by content from the used sources.

Graz, October 25th 2010

Abstract

The electron momentum density of a crystalline material determines many of its physical properties. A widely accepted experimental method to determine the electron momentum density is the positron annihilation spectroscopy, which has been very successful, especially in analysis of crystal defects. To gain a better understanding about the mechanisms that determine the Doppler profiles mesasured in those experiments and to get a link between theory and experiment, Doppler profiles have been calculated based on the many-particle problem in quantum mechanics. Starting point for all calculations are the Bloch functions determined by the full-potential linearized augmented plane wave (LAPW) band structure program *WIEN2k*. Further the electron momentum density and the electron-positron momentum density, that plays a crucial role in positron annihilation experiments, have been calculated using a linear density approximation (LDA) to describe the electron-positron correlation effects. From this data the corresponding one-dimensional Doppler profiles have been determined. Finally, other experimentally measurable quantities, such as the intrinsic magnetization and, especially, the positron lifetime have been derived.

Zusammenfassung

Theorie von Elektronen in Kristallen unter besonderer Berücksichtigung der Doppler-Spektroskopie

Das Ziel dieser Arbeit ist die Berechnung von experimentell zugänglichen Grössen ausgehend vom quantenmechanischen Modell der Vielteilchen-Schrödingergleichung der Elektronen in kristallinen Festkörpern. Das Hauptaugenmerk gilt hierbei der Berechnung der Impulsverteilung von Elektronen und Elektron-Positron-Paaren in Metallen. Als Grundlage hierfür werden die Ergebnisse von selbstkonsistenten Bandstrukturrechngen, die mit dem full potential linearized augmented plane wave (LAPW) Programm *WIEN2k* durchgeführt werden, herangezogen. Aus den erhaltenen Impulsverteilungen werden die materialspezifischen Comptonprofile und, vor allem, Dopplerprofile bestimmt, da diese in der experimentellen Methode der Positronen-Annihilationsspektroskopie eine direkte Messgrösse darstellen. Aus den Dopplerprofilen werden weitere experimentell zugängliche Grössen, wie etwa die Positronenlebensdauer oder die Magnetisierung berechnet.

Contents

1 Introduction **15**

2 General Aspects **17**

2.1 Introduction to Positron Physics 17

2.1.1 Compton scattering 17

2.1.2 Electron momentum density 18

2.1.3 Electron-positron annihilation probability 19

2.2 Positron Annihilation Experiments 21

2.2.1 Angular correlation spectroscopy 22

2.2.2 Coincidence Doppler broadening spectroscopy 22

2.2.3 Positron lifetime spectroscopy 24

2.3 Theoretical Treatment 24

2.3.1 The Bloch functions 24

3 Numerical Treatment **29**

3.1 The plane-wave representation 29

3.2 Electron-positron correlation: enhancement 30

3.3 Calculation of plane-wave coefficients of LAPW Bloch waves 33

3.4 Numerical evaluation of the EMD and EPMD in the plane-wave representation 39

4 Numerical Results **41**

4.1 Investigation of FeCu alloys 41

4.1.1 Paramagnetic treatment 41

4.1.2 Ferromagnetic calculations 53

4.1.3 Doppler profiles 60

5 Acknowledgments **71**

List of Figures

2.1 Scheme of Compton scattering [8]. 17

2.2 Scheme of the 2γ-annihilation in a perfect simple cubic lattice [13] 21

2.3 Comparison of one-dimensional Doppler profiles for GaAs, measured with a single dectector system and a coincidence measuring system. Using CDB, the peak-to-background ratio is improved by approximately two orders of magnitude [16]. 23

4.1 Nonpolarized density of states (DOS) for fcc $\mathrm{Fe}_x\mathrm{Cu}_{100-x}$ alloys for $x = 0$ (a), 25 (b), 50 (c), 75 (d) and 100 (e). The zero-energy represents the Fermi level. 43

4.2 Nonpolarized density of states (DOS) for bcc $\mathrm{Fe}_x\mathrm{Cu}_{100-x}$ alloys for $x = 0$ (a), 25 (b), 50 (c), 75 (d) and 100 (e). The zero-energy represents the Fermi level. 44

4.3 One-dimensional Compton profile for fcc Cu along the [100]-direction. All semi-core and valence electrons have been considered for various numbers of plane-wave coefficients from about 500 up to 2500. The desired convergence up to approximately 50 mrad is reached at about 2000 plane-waves. 45

4.4 One-dimensional Compton profile for bcc $\mathrm{Fe}_{25}\mathrm{Cu}_{75}$ along the [111]-direction. All semi-core and valence electrons have been considered for various numbers of plane-wave coefficients from about 3000 up to 7000. The desired convergence up to approximately 50 mrad is finally reached at about 6000 plane-waves. 46

4.5 One-dimensional Compton profile for fcc Cu along the [100]-direction for different bands. The valence states (3d and 4s) can not be separated. . . 47

4.6 One-dimensional Compton profile for bcc $\mathrm{Fe}_{25}\mathrm{Cu}_{75}$ along the [111]-direction for different bands. The valence states (3d and 4s) can not be separated. 47

4.7 1D-Compton profiles for bcc $\mathrm{Fe}_x\mathrm{Cu}_{1-x}$ alloys along the [100]-direction. . 49

4.8 1D-Compton profiles for bcc $\mathrm{Fe}_x\mathrm{Cu}_{1-x}$ alloys along the [110]-direction. . 50

4.9 1D-Compton profiles for fcc Fe_xCu_{1-x} alloys along the [100]-direction. . . 50
4.10 1D-Compton profiles for fcc Fe_xCu_{1-x} alloys along the [110]-direction. . . 51
4.11 1D-Compton profiles for $Fe_{100}Cu_0$, $Fe_{50}Cu_{50}$ and Fe_0Cu_{100} alloys along the [110]-direction. All curves are normalized to the same area. 52
4.12 Nonpolarized density of states (DOS) for the d-parts of Fe_xCu_{100-x} alloys as given in table 4.4, separated into their Cu (red line) and Fe (blue line) contributions. The zero-energy represents the Fermi level. 54
4.13 Normalized 1D-Compton profiles for ferromagnetic $Fe_{1-x}Cu_x$ alloys according to table (4.4) along the [100]-direction. 55
4.14 1D-Compton profiles for ferromagnetic $Fe_{100}Cu_0$ along the [100]-direction. 56
4.15 1D-Compton profiles for ferromagnetic $Fe_{75}Cu_{25}$ along the [100]-direction. 56
4.16 1D-Compton profiles for ferromagnetic bcc $Fe_{50}Cu_{50}$ along the [100]-direction. 57
4.17 1D-Compton profiles for ferromagnetic bcc $Fe_{50}Cu_{50}$ along the [100]-direction. 57
4.18 1D-Compton profiles for ferromagnetic bcc $Fe_{25}Cu_{75}$ along the [100]-direction. 58
4.19 Magnetic moments of $Fe_{1-x}Cu_x$ determined from the one-dimensional Compton profiles. The blue graph represents the magnetic moment averaged over all atoms in the unit cell, the red one shows the magnetic moment at the Fe sites. 59
4.20 One-dimensional Doppler profiles for Cu along the [100]-direction according to the independent particle model and different numbers of electron-positron Fourier coefficients (eq. 3.5). 61
4.21 Schematic demonstration of the convolution of the electron-positron plane-wave coefficients a^{ep} according to eq. 3.5. The black curves represent the electron plane-waves, the red ones mean the positron plane-waves. Left: correct convolution for a small K; right: erroneous convolution for a large K [20]. 62
4.22 One-dimensional Doppler profiles for $Fe_{25}Cu_{75}$ (3s+3p) along the directions [100], [110] and [111], according to the IPM (without any enhancement), calculated by using different numbers of electron-positron plane-wave coefficients from a number of 6859 electron plane-wave coefficients. 62
4.23 One-dimensional Doppler profile for Fe_xCu_{1-x} alloys along the [100]-direction according to the independent particle model (without any enhancement). All curves are normalized to the same area. 63
4.24 One-dimensional Compton profile for Fe_xCu_{1-x} alloys along the [100]-direction. All curves are normalized to the same area. 63

4.25 One-dimensional Doppler profiles for Cu along the [100]-direction using the different enhancement factors given in sec. 3.2 (BN=eq. 3.12, PSN=eq. 3.13, BPTN=eq. 3.14). τ means the bulk lifetime according to eq. 2.10. 65

4.26 One-dimensional Doppler profiles for Cu along the [100]-direction using the different enhancement factors given in sec. 3.2 (BN=eq. 3.12, PSN=eq. 3.13, BPTN=eq. 3.14). τ means the bulk lifetime according to eq. 2.10. 65

4.27 One-dimensional Compton and Doppler profiles for Cu along the [100]-direction. 66

4.28 One-dimensional Doppler profiles for Cu along the [100]-direction using the enhancement factor suggested in Ref. [19] (eq. 3.12). 67

4.29 One-dimensional Doppler profiles for Cu along the [100]-direction according to the IPM. 68

4.30 One-dimensional Compton profiles for Cu along the [100]-direction. . . . 68

4.31 Dependence of positron lifetime τ in $\mathrm{Fe}_{1-x}\mathrm{Cu}_x$ alloys to the fraction of Cu x, determined according to eq. 2.10, using the enhancement factor suggested in Ref. [19] (eq. 3.12). 69

1 Introduction

The electron momentum density distribution in crystalline materials determines a huge variety of physical properties. A widely accepted experimental method to investigate the electron momentum density is the positron annihilation spectroscopy [1], [2]. This method is very successful, especially in detecting crystal defects and any other kind of irregularities. The main advantage of positron annihilation experiments compared to Compton spectroscopy (see Refs. [3], [4]) is the fact that the positron is a charged particle, and hence, more attracted to crystal defects, such as impurities or vacancies, since any kind of crystal defects changes the local charge distribution. The most common experimental methods are the Doppler broadening technique, the angular correlation measurements and the positron lifetime measurements [5]. In order to gain a better understanding of the effects that determine the experimentally achieved data, the goal of this work is to get a link between *ab initio* theory and experiment. Starting point for all calculations made in this work is the quantum-mechanical model, hence, the many-particle Schrödinger equation for solid state materia. The Schrödinger equation is solved using the self-consistent full-potential LAPW program *WIEN2k* [6]. From these data the electron momentum density and further the electron-positron momentum density are derived using the independent particle model (IPM) and state-independent enhancement factors according to the linear density approximation (LDA) to describe electron-positron correlation effects. Finally the corresponding Doppler profiles and other experimentally measurable quantities, such as the magnetization or the positron lifetime are calculated. The goal of the calculations was to get reliable one-dimensional Doppler profiles for the investigated materials up to a momentum region of about $q = 50$ mrad, since this is the range where modern angular-correlation experiments are feasible and most of the information concerning crystal defects is detected in this high-momentum region. The investigated materials are (meta-)stable $\mathrm{Fe}_{100-x}\mathrm{Cu}_x$ alloys (with x=0, 25, 50, 75 and 100), that are assumed to form highly symmetric, perfect structures without any crystal defects. At first, two series have been considered, one in a bcc realization with the lattice constant such as for pure iron, the second series being in an fcc lattice with the lattice constant of pure copper. Since not all of these structures are stable in nature (see Wang et. al. [7]), only for a fraction of Cu $x \leq 50$ the bcc realization has further been treated while for $x \geq 50$ only the fcc realization has been taken into account. Using a generalized gradient approximation (GGA), these authors have further optimized the values for the lattice constants, which have been used in this thesis instead of the fixed ones described above. In the discussion of the results, especially the contributions of different electron bands to the total profiles are treated, with special emphasis to the 3d bands of Fe and Cu. These bands play a major role in determining the physical properties of a metal, especially in iron (and other 3d transition metals), where they cross the Fermi level, and are therefore responsible for electric conductivity. Further, the fact that these bands are not completely occupied in case of Fe determines the ferromagnetism of this metal. Finally, the positron lifetime in the investigated FeCu alloys has been calculated by numerical integration of the Doppler profiles and the values for pure Fe and Cu have been compared with the results of other calculations using the local density approximation as well as with experimental data.

Chapter 2 of this thesis presents a short summary of its theoretical basis and is mainly taken from the literature (see the list of references at the end of this work).

The chapters 3 and 4, however, contain basically new and original connections and results of the author.

2 General Aspects

2.1 Introduction to Positron Physics

In this chapter a short overview of the fundamentals to be treated in this work will be given.

2.1.1 Compton scattering

Compton scattering means an inelastic scattering process of a high energy photon (e.g X-Ray or γ photon) and an electron in the outer shell of an atom (Fig. 2.1):

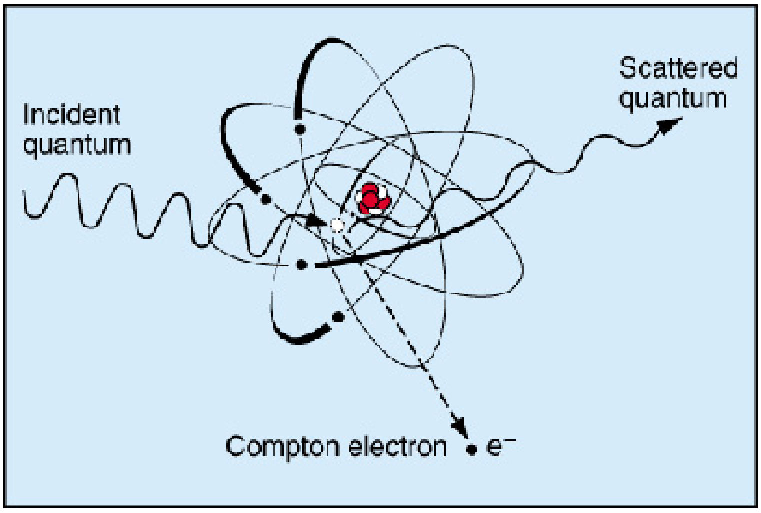

Figure 2.1: Scheme of Compton scattering [8].

In this process the electron is emitted from the shell while the incident photon is scattered inelastically. Thus, the photon changes its momentum and loses energy. The measuring quantity in Compton spectroscopy is the intensity of scattered photons within the solid angle $d\Omega$ which corresponds to the cross section (eq. 2.1) [4]

$$\frac{d\sigma}{d\Omega} \propto J^{Compton}(q, \mathbf{e}) = \int d^3p\rho(\mathbf{p})\delta(\mathbf{p}\cdot\mathbf{e} - q), \tag{2.1}$$

where $\mathbf{e} = \frac{\mathbf{q}}{|\mathbf{q}|}$ is the unit vector in direction of the scattered photons to be measured. This direction needs to be constant during the measurement, $q =\mid \mathbf{q} \mid$ means the measured contributions of this vector which correspond to the wavelengths of the Compton photons. This way one obtains a so-called one-dimensional Compton profile $J^{Compton}(q, \mathbf{e})$ for each direction to be measured. So, in eq. 2.1, there is one measurable quantity $J^{Compton}(q, \mathbf{e})$ on the left hand side while on the right hand side the function $\rho(\mathbf{q})$ represents the momentum distribution of the electrons in the solid state body. Integration of eq. 2.1 yields

$$\int_{-\infty}^{\infty} dqJ^{Compton}(q, \mathbf{e}) = \int d^3p\rho(\mathbf{p}). \tag{2.2}$$

Of course, such an integration of the electron momentum density over momentum space results in the number of electrons in the crystal. Usually, however, one normalizes the one-dimensional Compton profile such that

$$\int_{-\infty}^{\infty} dqJ^{Compton}(q, \mathbf{e}) = \int d^3p\rho(\mathbf{p}) = \gamma, \tag{2.3}$$

with γ being the number of electrons in the unit cell.

2.1.2 Electron momentum density

The evaluation of the electron momentum density (EMD) in crystalline solid state bodies is a very complex problem in computational physics. The easiest simplification hereby is to use the *independent particle model* (IPM, see e.g. Ref. [9]) which is given in eq. 2.4

$$\rho(\mathbf{p}) = 2\frac{1}{(2\pi)^3}\frac{\Omega_0}{\Omega}\sum_n\sum_{\mathbf{k}}^{BZ}\sum_{\mathbf{K}}\Theta(\epsilon_F - \epsilon_{n,\mathbf{k}}) \mid \int_\Omega d^3re^{-i\mathbf{p}\cdot\mathbf{r}}\psi_{n,\mathbf{k}}(\mathbf{r}) \mid^2 \delta_{\mathbf{k},\mathbf{p}-\mathbf{K}} \tag{2.4}$$

where Ω and Ω_0 are the volumes of the crystal and the unit cell, $\psi_{n,\mathbf{k}}$ mean the wave functions and $\epsilon_{n,\mathbf{k}}$ the energy eigenvalues of the electrons which can be obtained from band structure calculations. The quantity

$$|\int_{\Omega} d^3r\, \mathrm{e}^{-i\mathbf{p}\cdot\mathbf{r}}\, \psi_{n,\mathbf{k}}(\mathbf{r})|^2 \tag{2.5}$$

means the square of the Fourier transform of the Bloch function of the electron state $|n, \mathbf{k} >$ which represents the probability distribution of the Bloch function $\psi_{n,\mathbf{k}}(\mathbf{r})$ in momentum space with regard to the wave number $\mathbf{p}$. For $\mathbf{p}$ is a vector of the extended reciprocal space, and $\mathbf{k}$ is reduced to the first Brillouin zone, the Kronecker delta $\delta_{\mathbf{k},\mathbf{p}-\mathbf{K}}$ accepts only one term of the double sum $\sum_{\mathbf{k}} \sum_{\mathbf{K}}$, because there is only one possibility to define an average vector $\mathbf{p}$ as sum of a Brillouin zone vector and a reciprocal-lattice vector. Finally, the Heaviside function in eq. 2.4 arises from the fact that only electrons in occupied states, i.e., with energies lower than the Fermi energy ϵ_F contribute to the momentum density.

2.1.3 Electron-positron annihilation probability

When a positron emitted from an applicable radioactive source (e.g. Na-22, Cu-64, Co-58,...) penetrates a crystal, numerous collision processes between the positron on the one hand side and metallic ions and valence electrons on the other hand will occur until the positron is decelerated from its initial energy (some 100 keV) to the thermal energy of the electrons in the crystal. This process, called thermalization, happens during a few picoseconds [5]. Such a thermalized positron has a certain time (positron bulk lifetime) to move within the crystal (including further interactions with the crystal lattice and - preferably - the valence electrons) before it annihilates, as an anti-particle of an electron, with an electron in the metal. In this annihilation process the mass of the electron-positron pair is converted to energy according to Einstein's mass-energy equivalence. In most cases this energy is emitted by two photons with an energy of 511 keV each, what is called a 2γ-annihilation process. The time between the emission of a positron and its annihilation is called the positron lifetime which is typically a few hundred picoseconds in solid metals. In real experiments, the time between the emission of photons from the source is much larger than the positron lifetime, hence, there is only one positron in the crystal. Therefore, the positron can be assumed to be in its ground state after the thermalization process.

A quantity of particular interest in positron physics is the probability of the positron to annihilate with an electron in the metal. This probability is called the annihilation rate $R(\mathbf{p})$ and depends on the annihilation momentum $\mathbf{p}$ which is the sum of the momenta of the annihilating particles:

$$\mathbf{p} = \mathbf{p}_e + \mathbf{p}_p. \tag{2.6}$$

As a result of quantum electrodynamics (see, e.g. Refs. [1], [2]), the annihilation rate is directly related to the momentum density of the annihilating electron-positron pair $\rho_{ep}(\mathbf{p})$ (eq. 2.7).

$$R(\mathbf{p}) = \frac{r_0^2 \pi c}{\Omega_0} \rho_{ep}(\mathbf{p}), \tag{2.7}$$

where r_0 is the classical electron radius and c is the speed of light.

Momentum density of electron-positron pairs: Since the accurate derivation of $\rho_{ep}(\mathbf{p})$ is rather complicated, the Coulomb interaction between the electron and the positron is often neglected (independent particle model, IPM). Assuming that the local density of positrons in the crystal is much smaller than the density of electrons, the electron-positron momentum density (EPMD) in the independent particle model reads [1]

$$\rho_{ep}(\mathbf{p}) = \frac{2\Omega_0}{(2\pi)^3} \sum_n \sum_{\mathbf{k}}^{BZ} \sum_{\mathbf{K}} \Theta(\epsilon_F - \epsilon_{n,\mathbf{k}}) \mid \int_\Omega d^3r \mathrm{e}^{-i\mathbf{p}\cdot\mathbf{r}} \psi_{n,\mathbf{k}}(\mathbf{r}) \psi_+(\mathbf{r}) \mid^2 \delta_{\mathbf{k},\mathbf{p}-\mathbf{K}}. \tag{2.8}$$

Formally, a comparison of the above formula with the corresponding electron momentum density (eq. 2.4) obtains that the Fourier integral of the electron state $\psi_{n,\mathbf{k}}(\mathbf{r})$ is replaced by the Fourier integral of the overlap of the electron Bloch state $\psi_{n,\mathbf{k}}(\mathbf{r})$ and the positron ground state wave function $\psi_+(\mathbf{r})$.

The normalization has been chosen such that in case of a positron that is uniformly distributed over the whole crystal, thus

$$\psi_+(\mathbf{r}) = \frac{1}{\sqrt{\Omega}}, \tag{2.9}$$

eq. 2.8 turns out to be the electron momentum density as given in eq. 2.4. Using this normalization and eq. 2.7 yields another essential relation (eq. 2.10):

$$\int d^3p R_{2\gamma}(\mathbf{p}) = \frac{r_0^2 \pi c}{\Omega_0} \int d^3p \rho_{ep}(\mathbf{p}) = \frac{1}{\tau}, \tag{2.10}$$

where τ is the bulk lifetime of a positron in ground state in a perfect crystal.

The advanced EPMD-formula: Enhancement: In eq. 2.8, the independent particle approximation neglects the Coulomb interaction between the positron and the electrons.

This formula just contains the product of the wave functions of the annihilating particles, but the particles do not mutually influence each other. On the one hand, such a neglect of a major force, such as the Coulomb interaction, strongly decreases the quality of eq. 2.8, but on the other hand the exact implementation of the electron-positron correlation would get too complicated to handle [10],[11]. Therefore some authors suggested the compromise to describe the electron-positron correlation effect (enhancement effect) approximately by the local multiplicative factor $g_{n,\mathbf{k}}(\mathbf{r})$ in the electron-positron momentum equation [12]:

$$\rho_{ep}(\mathbf{p}) = \frac{2\Omega_0}{(2\pi)^3} \sum_n \sum_{\mathbf{k}}^{BZ} \sum_{\mathbf{K}} \Theta(\epsilon_F - \epsilon_{n,\mathbf{k}}) \mid \int_\Omega d^3 r \mathrm{e}^{-i\mathbf{p}\cdot\mathbf{r}} \psi_{n,\mathbf{k}}(\mathbf{r}) \sqrt{g_{n,\mathbf{k}}(\mathbf{r})} \psi_+(\mathbf{r}) \mid^2 \delta_{\mathbf{k},\mathbf{p}-\mathbf{K}} \tag{2.11}$$

Further information and a detailed treatment of the enhancement factor $g_{n,\mathbf{k}}(\mathbf{r})$ are given in section 3.2.

2.2 Positron Annihilation Experiments

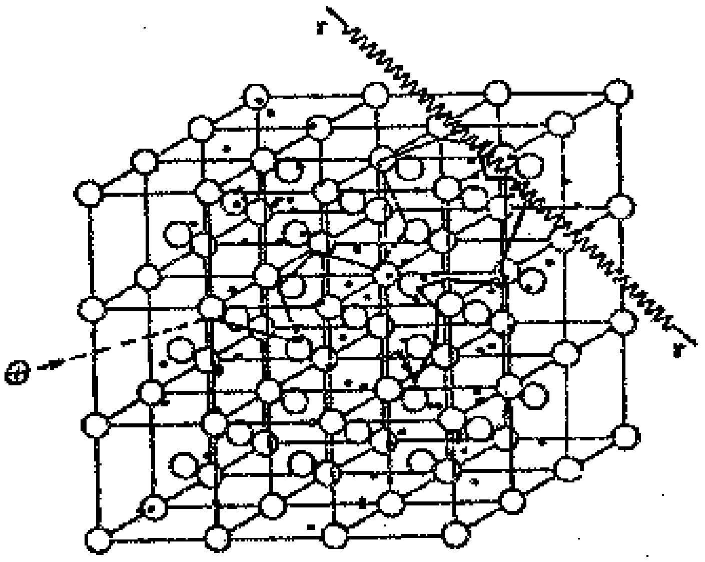

Figure 2.2: Scheme of the 2γ-annihilation in a perfect simple cubic lattice [13]

The diagram (fig. 2.2) demonstrates some fundamental aspects of a 2γ-annihilation within an ideal crystal: an electron-positron pair with a total momentum $\hbar\mathbf{p}$ annihilates into two photons with the momentum-dependent annihilation rate $R_{2\gamma}(\mathbf{p})$. According to equation 2.7, this quantity is proportional to the electron-momentum density $\rho_{ep}(\mathbf{p})$.

Unfortunately, there exists no experimental method that enables a direct measurement of $R_{2\gamma}$ as a function of its three independent arguments p_x, p_y, and p_z. In the following, the three most important positron annihilation experiments are shortly described, more detailed information about these methods can be found in the literature.

2.2.1 Angular correlation spectroscopy

This method is based on the measurement of the deviations Θ of the emitted annihilation photons from 180 degrees. This angle is due to the transversal component p_T of the total momentum of the annihilating electron-positron pair and reads

$$\Theta = \frac{p_T}{mc}. \tag{2.12}$$

In realistic experiments, this small angle is measured in units of milliradiants (mrad): equation 2.12 gives the explanation why (in Compton and positron spectroscopy, and also in this thesis) momenta are given in mrad (see chapter 4).

Angular correlation (AC) spectroscopy can be realized by (very extensive) 2D experiments, leading to the two-dimensional angular correlation spectrum

$$N(p_x, p_y) \propto \int dp_z R_{2\gamma}(\mathbf{p}), \tag{2.13}$$

whereas 1D experiments in the so-called *long-slit geometry* lead to the one-dimensional AC profile

$$N(p_z) \propto \int dp_x dp_y R_{2\gamma}(\mathbf{p}). \tag{2.14}$$

2.2.2 Coincidence Doppler broadening spectroscopy

This method is based on the fact that the motion of the electron-positron pair causes a Doppler shift on the energy of the annihilation radiation which is proportional to the longitudinal component p_L of the total electron-positron momentum as

$$\Delta E = c\frac{p_L}{2}. \tag{2.15}$$

The result of such experiments is the one-dimensional Doppler profile

$$J^{Doppler}(q, \mathbf{e}) \propto d^3 p R_{2\gamma}(\mathbf{p}) \delta(\mathbf{p} \cdot \mathbf{e} - q). \tag{2.16}$$

Originally, Doppler spectroscopy has been performed using a single-detector system. However, *state-of-the-art* is the so-called coincidence Doppler broadening technique (CDB). In this alignment, two detectors that are placed diametrically with respect to the specimen are used. Further they operate in coincident way, thus a signal is only converted if it is detected in both detectors simultaneously. The main advantage of this method in comparison to the single detector system is an improved peak-to-background ratio by about two orders of magnitude (fig. 2.3). This high sensitivity is an essential condition for a reliable experimental determination of electron-positron momentum densities in the high-momentum region (> 35mrad) where the core electrons play the major role. More details about CDB can be found, e.g., in Refs. [14], [15].

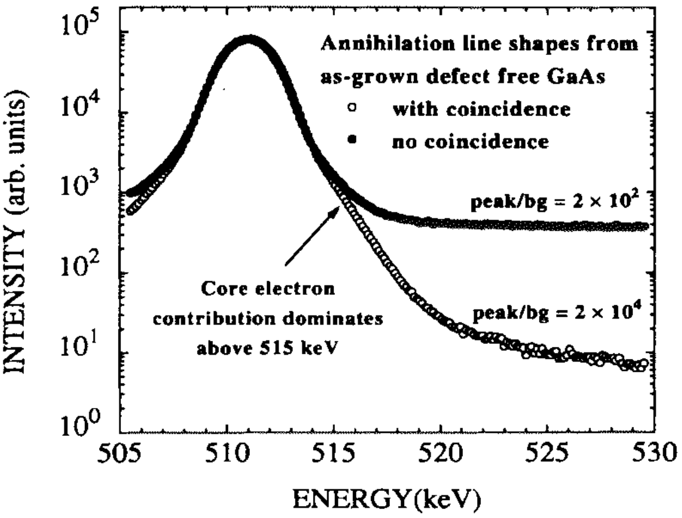

Figure 2.3: Comparison of one-dimensional Doppler profiles for GaAs, measured with a single dectector system and a coincidence measuring system. Using CDB, the peak-to-background ratio is improved by approximately two orders of magnitude [16].

2.2.3 Positron lifetime spectroscopy

In positron lifetime spectroscopy, the quantity to be measured is the time between the emission of the positron from the source and the emission of the photons that are generated in the electron-positron annihilation process within the specimen. The thermalization process happens within a very short period of time with respect to the bulk lifetime of a positron (time between thermalization and annihilation). Therefore, the measured time between the emission of the positron and the emission of the photons, that arise from the annihilation process, is denoted as the bulk lifetime in positron lifetime spectroscopy. The correlation between the positron bulk lifetime, the annihilation rate and the electron-positron momentum density is given in eq. 2.10. For further information see, e.g., Ref. [5].

2.3 Theoretical Treatment

2.3.1 The Bloch functions

The wave functions of the electrons $\psi_{n,\mathbf{k}}(\mathbf{r})$ and the positrons $\psi^{+}_{n,\mathbf{k}}(\mathbf{r})$ are calculated using single-particle Schrödinger equations based on the density functional theory (DFT) by Hohenberg et. al. [17] and Kohn et. al. [18]. According to the two-component density functional theory (see, e.g. Ref. [19]) the ground-state energy of the interacting electron-positron system can be written as a functional depending on the particle densities of electrons n^- and positrons n^+:

$$\begin{aligned}
E[n^-,n^+] &= \underbrace{\int d^3r v^-(\mathbf{r})n^-(\mathbf{r})}_{(1)} + \underbrace{\int d^3r v^+(\mathbf{r})n^+(\mathbf{r})}_{(2)} - \underbrace{e^2\int d^3r d^3r' \frac{n^-(\mathbf{r})n^+(\mathbf{r}')}{\mid \mathbf{r}-\mathbf{r}' \mid}}_{(3)} \\
&+ \underbrace{\frac{e^2}{2}\int d^3r d^3r' \frac{n^-(\mathbf{r})n^-(\mathbf{r}')}{\mid \mathbf{r}-\mathbf{r}' \mid}}_{(4)} + \underbrace{\frac{e^2}{2}\int d^3r d^3r' \frac{n^+(\mathbf{r})n^+(\mathbf{r}')}{\mid \mathbf{r}-\mathbf{r}' \mid}}_{(5)} \\
&+ \underbrace{T[n^-]}_{(6)} + \underbrace{T[n^+]}_{(7)} + \underbrace{E_{xc}[n^-,n^+]}_{(8)} \qquad (2.17)
\end{aligned}$$

The terms (1) and (2) describe the potential energy of the particles in the crystal potential, (3),(4) and (5) mean the Hartree-Potentials caused by the Coulomb interaction between the charged particles and (6) and (7) describe the kinetic energies of electrons and positrons. The last term (8) contains exchange and correlation effects:

$$E_{xc}[n^+, n^-] = E^-_{xc}[n^-] + E^+_{xc}[n^+] + E^{+-}_c[n^-, n^+], \tag{2.18}$$

where the first term describes the exchange-correlation effects between the electrons, the second one is for the positrons and the last term includes the electron-positron-correlations. In a real positron annihilation experiment, however, the number of positrons in the crystal n^+ is by many orders of magnitude smaller than the number of electrons n^-. A quite good approximation is to assume that there is only one positron interacting with the electrons in its proximity. As a consequence, all exchange and correlation effects between positrons can be neglected and eq. 2.18 reduces to

$$E_{xc}[n^+, n^-] = E^-_{xc}[n^-] + E^{+-}_c[n^-, n^+]. \tag{2.19}$$

According to Ref. [18], the electronic single-particle Schrödinger equations for the electron-positron system can be obtained by a variational ansatz

$$\left\{ \frac{\delta E[n^-, n^+]}{\delta n^-} - \epsilon_{n,\mathbf{k}} \right\} \psi_{n,\mathbf{k}}(\mathbf{r}) = 0 \tag{2.20}$$

as well as the single-particle Schrödinger equations for the positrons

$$\left\{ \frac{\delta E[n^-, n^+]}{\delta n^+} - \epsilon^+_{n,\mathbf{k}} \right\} \psi^+_{n,\mathbf{k}}(\mathbf{r}) = 0. \tag{2.21}$$

A combination of this ansatz with eq. 2.17 and eq. 2.19 leads to a system of coupled equations:

$$\begin{gathered} \left\{ -\frac{\hbar^2}{2m}\nabla^2 + v^-(\mathbf{r}) + v_H(\mathbf{r}) + \frac{\delta E^-_{xc}[n^-]}{\delta n^-} + \frac{\delta E^{+-}_c[n^-, n^+]}{\delta n^-} - \epsilon_{n,\mathbf{k}} \right\} \psi_{n,\mathbf{k}}(\mathbf{r}) = 0 \\ \left\{ -\frac{\hbar^2}{2m}\nabla^2 + v^+(\mathbf{r}) - v_H(\mathbf{r}) + \frac{\delta E^{+-}_c[n^-, n^+]}{\delta n^+} - \epsilon^+_{n,\mathbf{k}} \right\} \psi^+_{n,\mathbf{k}}(\mathbf{r}) = 0, \end{gathered} \tag{2.22}$$

where $v_H(\mathbf{r})$ is the Hartree-potential:

$$v_H(\mathbf{r}) = e^2 \int d^3r' \frac{n^-(\mathbf{r}') - n^+(\mathbf{r}')}{\mid \mathbf{r} - \mathbf{r}' \mid}. \tag{2.23}$$

At this point another approximation has to be done since the correlation between the functionals E^-_{xc} and E^{+-}_c and the particle densities is not known for inhomogenous electron gases as they appear in real crystals. Most band structure programs use the local density approximation (LDA):

$$E^-_{xc}[n^-] \approx \int d^3r \mu_{xc}(n^-(\mathbf{r}))n^-(\mathbf{r}) \tag{2.24}$$

and

$$E^{+-}_c[n^-, n^+] \approx \int d^3r \mu^{+-}_c(n^-(\mathbf{r}))n^+(\mathbf{r}), \tag{2.25}$$

where $\mu_{xc}(n^-(\mathbf{r}))$ is the exchange-correlation energy in a homogeneous electron gas and $\mu^{+-}_c(n^-(\mathbf{r}))$ describes the correlation energy in a homogeneous electron-positron gas. The variation of E^-_{xc} in the electronic variation equation (eq. 2.22) now yields

$$\frac{\delta E^-_{xc}[n^-]}{\delta n^-} \approx \mu_{xc}(n^-(\mathbf{r})) + \frac{\delta \mu^{+-}_{xc}(n^-)}{\delta n^-} n^-(\mathbf{r}) = v^{LDA}_{xc}(n^-(\mathbf{r})), \tag{2.26}$$

which is the LDA-approximation for the exchange-correlation part. Further one gets

$$\frac{\delta E^{+-}_c[n^-, n^+]}{\delta n^-} \approx \frac{\delta \mu^{+-}_c(n^-)}{\delta n^-} n^+(\mathbf{r}) \tag{2.27}$$

and

$$\frac{\delta E^{+-}_c[n^-, n^+]}{\delta n^+} \approx \mu^{+-}_c(n^-(\mathbf{r})). \tag{2.28}$$

After inserting this in eq. 2.22 the electronic equation turns into

$$\left\{ -\frac{\hbar^2}{2m}\nabla^2 + v^-(\mathbf{r}) + v_H(\mathbf{r}) + v^{LDA}_{xc}(n^-(\mathbf{r})) + \frac{\delta \mu^{+-}_c(n^-)}{\delta n^-} n^+(\mathbf{r}) \right\} \psi_{n,\mathbf{k}}(\mathbf{r}) = \epsilon_{n,\mathbf{k}} \psi_{n,\mathbf{k}}(\mathbf{r}) \tag{2.29}$$

and the equation for the positron states

$$\left\{ -\frac{\hbar^2}{2m}\nabla^2 + v^+(\mathbf{r}) - v_H(\mathbf{r}) + \mu^{+-}_c(n^-(\mathbf{r})) \right\} \psi^+_{n,\mathbf{k}}(\mathbf{r}) = \epsilon^+_{n,\mathbf{k}} \psi^+_{n,\mathbf{k}}(\mathbf{r}). \tag{2.30}$$

The particle densities are now formed by the eigenfunctions of these equations. Further, according to the previously described *one-positron-in-ground-state* approximation, one has $n = 1$ and $\mathbf{k} = 0$ for $\psi^+(\mathbf{r})$. The particle densities for electrons and positrons therefore are

$$n^-(\mathbf{r}) = \sum_n \sum_{\mathbf{k}}^{BZ} \mid \psi_{n,\mathbf{k}}(\mathbf{r}) \mid^2 \Theta(\epsilon_F - \epsilon_{n,\mathbf{k}})$$

$$\text{and} \tag{2.31}$$

$$n^+(\mathbf{k}) = \mid \psi^+_{1,\mathbf{0}}(\mathbf{r}) \mid^2 =: \mid \psi^+(\mathbf{r}) \mid^2 .$$

As mentioned above, there is only one positron assumed to be in the crystal. Hence, in all terms containing the positron density explicitely,

$$n^+(\mathbf{r}) \to 0$$

is a convenient approximation. Inserting this in eq. 2.29 and eq. 2.23 yields the simplified equations

$$\left\{ -\frac{\hbar^2}{2m}\nabla^2 + v^-(\mathbf{r}) + v_H(\mathbf{r}) + v_{xc}^{LDA}(n^-(\mathbf{r})) \right\} \psi_{n,\mathbf{k}}(\mathbf{r}) = \epsilon_{n,\mathbf{k}} \psi_{n,\mathbf{k}}(\mathbf{r}), \tag{2.32}$$

$$\left\{ -\frac{\hbar^2}{2m}\nabla^2 + v^+(\mathbf{r}) - v_H(\mathbf{r}) + \mu_c^{+-}(n^-(\mathbf{r})) \right\} \psi^+_{n,\mathbf{k}}(\mathbf{r}) = \epsilon^+_{n,\mathbf{k}} \psi^+_{n,\mathbf{k}}(\mathbf{r}). \tag{2.33}$$

and

$$v_H(\mathbf{r}) = e^2 \int d^3r' \frac{n^-(\mathbf{r}')}{\mid \mathbf{r} - \mathbf{r}' \mid}. \tag{2.34}$$

The Schrödinger equations for the electrons and the positrons are no longer coupled and a self-consistent solution of the above problem is strongly simplified.

3 Numerical Treatment

3.1 The plane-wave representation

To obtain the one-dimensional Doppler and Compton profiles it is now necessary to evaluate the formula for the electron momentum density distribution (EMD) as given in eq. 2.4. Therefore one has to know the electron Bloch function $\psi_{n,\mathbf{k}}(\mathbf{r})$. This function is calculated using the full-potential LAPW program *WIEN2k* [6] and is represented in form of a linear expansion of the functional basis $\varphi_{\mathbf{k}}^{LAPW}(\mathbf{r})$. These functions, however, are rather complicated, hence, it is convenient to express the LAPW-Bloch function as a Fourier series

$$\psi_{n,\mathbf{k}}(\mathbf{r}) = \sum_{\mathbf{G}} a_{n,\mathbf{k}}^{LAPW}(\mathbf{G})\varphi_{\mathbf{k}}^{LAPW}(\mathbf{r}) = \frac{1}{\sqrt{\Omega}} \sum_{\mathbf{G}} a_{n,\mathbf{k}}^{PW}(\mathbf{G}) \mathrm{e}^{i(\mathbf{k}+\mathbf{G})\cdot\mathbf{r}}, \tag{3.1}$$

where $\mathbf{G}$ is a vector of the reciprocal-lattice of the crystal. Since a Fourier expansion is based on plane waves, the corresponding coefficients $a_{n,\mathbf{k}}^{PW}(\mathbf{G})$ are called plane-wave coefficients. Inserting eq. 3.1 into eq. 2.4 and performing some fundamental mathematical manipulations yields the formula for the electron momentum density (EMD) in the plane-wave representation [20]:

$$\rho(\mathbf{p}) = \frac{2\Omega_0}{(2\pi)^3} \sum_{n} \sum_{\mathbf{k}}^{BZ} \Theta(\epsilon_F - \epsilon_{n,\mathbf{k}}) \sum_{\mathbf{K}} \delta_{\mathbf{k},\mathbf{p}-\mathbf{K}} \mid a_{n,\mathbf{k}}^{PW}(\mathbf{K}) \mid^2 . \tag{3.2}$$

Further one gets for the plane-wave representation of the uniformly distributed positron

$$\psi_{+}(\mathbf{r}) = \frac{1}{\sqrt{\Omega}} \sum_{\mathbf{G}'} b_{+}^{PW}(\mathbf{G}') \mathrm{e}^{i\mathbf{G}'\cdot\mathbf{r}}. \tag{3.3}$$

Inserting this and the plane-wave representation for electrons (eq. 3.1) into eq. 2.8, one finally gets

$$\rho_{ep}(\mathbf{p}) = \frac{2\Omega_0}{(2\pi)^3} \sum_n \sum_{\mathbf{k}}^{BZ} \Theta(\epsilon_F - \epsilon_{n,\mathbf{k}}) \sum_{\mathbf{K}} \delta_{\mathbf{k},\mathbf{p}-\mathbf{K}} \mid a^{ep}_{n,\mathbf{k}}(\mathbf{K}) \mid^2, \tag{3.4}$$

the plane-wave representation for the electron-positron momentum density according to the independent particle approximation where

$$a^{ep}_{n,\mathbf{k}}(\mathbf{K}) := \sum_{\mathbf{G}} a^{PW}_{n,\mathbf{k}}(\mathbf{G}) b^{PW}_{+}(\mathbf{K}-\mathbf{G}) \tag{3.5}$$

are the electron-positron Fourier coefficients. In the following calculations the transformation of the Bloch functions for the electrons as a result of the band structure calculation performed by the full-potential LAPW program *WIEN2k* to the plane-wave representation is done in the program *main_PWcalc.exe* and for the positron in the program *main_positron.exe* as described in section 3.3. The further calculation of the electron-positron Fourier coefficients is performed by the program *IPM_coeff.exe*. For details on the programs mentioned above, see Ref. [13].

3.2 Electron-positron correlation: enhancement

In the positron literature, and also in this thesis, the equations 3.4 and 3.5 are denoted *electron-positron momentum density according to the independent particle model.*
What does this term IPM mean? In principle, this means that the two-particle electron-positron wave function $\psi_{ep}(\mathbf{r}_e, \mathbf{r}_p)$ can be separated into its electron and positron part, i.e.,

$$\psi_{ep}(\mathbf{r}_e, \mathbf{r}_p) = \psi_e(\mathbf{r}_e) \cdot \psi_p(\mathbf{r}_p) \tag{3.6}$$

(compare equation 2.8), where $\psi_e(\mathbf{r})$ and $\psi_p(\mathbf{r})$ are solutions of the separated Schrödinger equations 2.32 and 2.33. This meaning of IPM does obviously not mean that there is no interaction between the positron and the surrounding electrons, since there is a term $-v_H(\mathbf{r})$ in the Hamiltonian of eq. 2.33 which describes a Hartree interaction between the positron and the electron gas $\mu^-(\mathbf{r})$, and there is even the electron-positron correlation term $\mu_c^{+-}(n^-(\mathbf{r}))$ in the LDA in this Hamiltonian. The functional relation between the electron-positron correlation potential $\mu_c^{+-}(n^-(\mathbf{r}))$ and the electron density $n_e(\mathbf{r})$ has been intensively investigated during the last decades, leading, e.g., to theoretical results by Arponnen and Pajanne [21] that have been parametrized by Boronski and Nieminen [19] with the following results:

$$\mu_c^{+-}(n^-(\mathbf{r})) = v_{ep}(\mathbf{r}_s) \tag{3.7}$$

and

$$\begin{aligned} v_{ep}(r_s) &= -\frac{1.56}{\sqrt{r_s}} + (0.051 \ln r_s - 0.081)\ln r_s + 1.14 \text{ for } r_s \leq 0.302. \\ v_{ep}(r_s) &= -0.92305 - \frac{0.05459}{r_s^2} \text{ for } 0.302 \leq r_s \leq 0.56, \\ v_{ep}(r_s) &= -\frac{13.1511}{(r_s+2.5)^2} + \frac{2.8655}{r_s+2.5} - 0.6298 \text{ for } 0.56 \leq r_s \leq 8.0, \\ v_{ep}(r_s) &= -179856.2768 n_e^2 + 186.4207 n_e - 0.524 \text{ for } 8.0 \leq r_s \leq \infty, \end{aligned} \tag{3.8}$$

with

$$r_s(\mathbf{r}) = \left[\frac{3}{4\pi n_e(\mathbf{r})}\right]^{1/3}. \tag{3.9}$$

The above equation is - in principle - only valid for $n_+ \to 0$, hence, for a single completely delocalized positron in a perfect crystal.

LDA correlation terms like eqs. 3.8 and 3.9 are entirely contained in the one-particle Schrödinger equations (and also in the investigation presented here), but their influence on the shape and area of the one-dimensional Doppler profiles is rather small. Much more important for the theory of positrons in electron gases is the so-called enhancement effect which is also a consequence of electron-positron correlation, but can not be realistically described by one-particle approximations. It is a real two-particle effect whose theory has been successfully formulated for the homogeneous electron gas (for a comprehensive summary, see e.g. Ref. [10]). For inhomogeneous electron gases, however, such a two-particle electron-positron correlation theory is extremely tedious and too complicated for the 'daily life' (see Ref. [11]).

A suitable approximation (but totally non-ab initio) of such an electron-positron enhancement goes back to several authors [12] leading to

$$\psi_{ep}(\mathbf{r}_e, \mathbf{r}_p) \approx \psi_{n,\mathbf{k}}(\mathbf{r})\sqrt{g_{n,\mathbf{k}}(\mathbf{r})}\psi_+(\mathbf{r}), \tag{3.10}$$

where $g_{n,\mathbf{k}}(\mathbf{r})$ refers to the change of the positron ground state due to the Coulomb correlation with an electron in the Bloch state $|n, \mathbf{k}>$. As a further approximation, many authors propose a state-independent ansatz for the electron-positron correlation function ($g_{n,\mathbf{k}}(\mathbf{r}) \approx g(\mathbf{r})$). Inserting this ansatz into the IPM formula for the electron-positron momentum density (eq. 2.8) yields

$$\begin{aligned}\rho_{ep}^{enh}(\mathbf{p}) &= \frac{2\Omega_0}{(2\pi)^3} \sum_n \sum_{\mathbf{k}}^{BZ} \sum_{\mathbf{K}} \Theta(\epsilon_F - \epsilon_{n,\mathbf{k}}) \delta_{\mathbf{p}-\mathbf{k},\mathbf{K}} \\ &\times \; | \int_\Omega d^3 r \mathrm{e}^{-i\mathbf{p}\cdot\mathbf{r}} \psi_{n,\mathbf{k}}(\mathbf{r}) \sqrt{g(\mathbf{r})} \psi_+(\mathbf{r})|^2, \end{aligned} \qquad (3.11)$$

For the function $g(\mathbf{r})$, several proposals have been made, the most common were proposed by Boronski and Nieminen [19]

$$g^{BN} = 1 + 1.23 r_s + 0.8295 r_s^{3/2} - 1.26 r_s^2 + 0.3286 r_s^{5/2} + r_s^3/6, \qquad (3.12)$$

by Puska, Seitsonen and Nieminen [22]

$$g^{PSN} = 1 + 1.23 r_s + 0.9889 r_s^{3/2} - 1.482 r_s^2 + 0.3956 r_s^{5/2} + r_s^3/6 \qquad (3.13)$$

and finally by Barbinielli, Puska, Torsti and Nieminen [23]

$$g^{BPTN} = 1 + 1.23 r_s - 0.0742 r_s^2 + r_s^3/6. \qquad (3.14)$$

In case of these state independent enhancement factors as given in eqs. 3.12-3.14 the enhanced positron wave function can be defined as

$$\psi_+^{enh}(\mathbf{r}) = \sqrt{g_{n,\mathbf{k}}(\mathbf{r})} \psi_+(\mathbf{r}). \qquad (3.15)$$

Obviously, for $g(\mathbf{r}) = 1$, eq. 3.11 reduces to the independent particle model (eq. 2.8).

3.3 Calculation of plane-wave coefficients of LAPW Bloch waves

As already given in sec. 3.1 the LAPW Bloch function can be expressed by a Fourier series (eq. 3.1) that defines the plane wave coefficients

$$\psi_{n,\mathbf{k}}(\mathbf{r}) = \frac{1}{\sqrt{\Omega}} \sum_{\mathbf{G}} a_{n,\mathbf{k}}(\mathbf{G})\, \mathrm{e}^{i(\mathbf{k}+\mathbf{G})\cdot\mathbf{r}}, \tag{3.16}$$

where $a_{n,\mathbf{k}}(\mathbf{G})$ is the desired plane-wave coefficient of the Bloch state $\psi_{n,\mathbf{k}}(\mathbf{r})$ according to the reciprocal-lattice vector $\mathbf{G}$ and Ω is the volume of the crystal. Resolving equation 3.16 with respect to the plane-wave coefficient $a_{n,\mathbf{k}}(\mathbf{G})$ yields

$$a_{n,\mathbf{k}}(\mathbf{G}) = \frac{1}{\sqrt{\Omega}} \int_{\Omega} d^3r\, \mathrm{e}^{-i(\mathbf{k}+\mathbf{G})\cdot\mathbf{r}}\, \psi_{n,\mathbf{k}}(\mathbf{r})\,. \tag{3.17}$$

Using the Bloch condition

$$\psi_{n,\mathbf{k}}(\mathbf{r}+\mathbf{R}) = \mathrm{e}^{i\mathbf{k}\cdot\mathbf{R}}\, \psi_{n,\mathbf{k}}(\mathbf{r})\,, \tag{3.18}$$

the integral in eq. 3.17 can be reduced to an integral over the volume of the unit cell Ω_0:

$$a_{n,\mathbf{k}}(\mathbf{G}) = \frac{\sqrt{\Omega}}{\sqrt{\Omega_0}} \int_{\Omega_0} d^3r\, \mathrm{e}^{-i(\mathbf{k}+\mathbf{G})\cdot\mathbf{r}}\, \psi_{n,\mathbf{k}}(\mathbf{r})\,. \tag{3.19}$$

The Bloch function calculated by the program *WIEN2k* is given by the LAPW expansion

$$\psi_{n,\mathbf{k}}(\mathbf{r}) = \sum_{i=1}^{z_1} c_{n,\mathbf{k}}(\mathbf{K}_i) \sum_{t} \sum_{\alpha} \Phi^{t,\alpha}_{\mathbf{k}+\mathbf{K}_i}(\mathbf{r}) \tag{3.20}$$

where the $c_{n,\mathbf{k}}(\mathbf{K}_i)$ are the coefficients with respect to the LAPW basis functions $\Phi^{t,\alpha}_{\mathbf{k}}(\mathbf{r})$. Further information and a detailed description of the LAPW basis functions obtained by the full-potential LAPW program *WIEN2k* are given in Ref. [24]. The basis functions have the following shape

$$\begin{aligned} \Phi^{t,\alpha}_{\mathbf{k}}(\mathbf{r}) \;&=\; \sum_{\ell=0}^{L} \sum_{-m}^{m} \Big[A^{t,\alpha}_{l,m}(\mathbf{k})\, u^{(t)}_{\ell}(|\mathbf{r}-\mathbf{r}_{t,\alpha}|, E_\ell) + B^{t,\alpha}_{l,m}(\mathbf{k})\, \dot{u}^{(t)}_{\ell}(|\mathbf{r}-\mathbf{r}_{t,\alpha}|, E_\ell) \Big] \\ &\times\; Y_{\ell,m}(\mathbf{r}-\mathbf{r}_{t,\alpha})\, \Theta(r^{(t)}_{MT} - |\mathbf{r}-\mathbf{r}_{t,\alpha}|) \end{aligned} \tag{3.21}$$

with

$$\dot{u}_\ell^{(t)}(\mathbf{r}) = \frac{du_\ell^{(t)}(\mathbf{r})}{dE_\ell} \tag{3.22}$$

for all non-overlapping muffin-tin spheres within the unit cell Ω_0. In equation 3.21, t means the t^{th} non-equivalent atom in the unit cell, while α means one of the equivalent atoms belonging to the group of t. Further, $\mathbf{r}_{t,\alpha}$ describes the position of the atom indicated by (t,α) and $\mathbf{r}_{MT}^{(t)}$ is the radius of the surrounding muffin-tin sphere. Outside of all muffin-tin spheres (in the so-called interstitial region), the LAPW basis function is simply given by the plane wave

$$\Phi_{\mathbf{k}}(\mathbf{r}) = \frac{1}{\sqrt{\Omega}}\,\mathrm{e}^{i\mathbf{k}\cdot\mathbf{r}}\,. \tag{3.23}$$

The parameters A and B that in equation 3.21 are chosen such that no discontinuitites of Φ and the first derivation of Φ with respect to $\mathbf{r}$ occur on the surface of the muffin-tin sphere, hence,

$$A_{\ell,m}^{t,\alpha}(\mathbf{k}+\mathbf{K}) = \frac{4\pi r_{MT}^{(t)2}}{\sqrt{\Omega}} i^\ell\, Y_{\ell,m}^*(\mathbf{k}+\mathbf{K})\,\mathrm{e}^{i(\mathbf{k}+\mathbf{K})\cdot\mathbf{r}_{t,\alpha}}\, a_\ell^{(t)}(\mathbf{k}+\mathbf{K}) \tag{3.24}$$

and

$$B_{\ell,m}^{t,\alpha}(\mathbf{k}+\mathbf{K}) = \frac{4\pi r_{MT}^{(t)2}}{\sqrt{\Omega}} i^\ell\, Y_{\ell,m}^*(\mathbf{k}+\mathbf{K})\,\mathrm{e}^{i(\mathbf{k}+\mathbf{K})\cdot\mathbf{r}_{t,\alpha}}\, b_\ell^{(t)}(\mathbf{k}+\mathbf{K}) \tag{3.25}$$

with

$$\alpha_\ell^{(t)}(\mathbf{k}+\mathbf{K}) = j'_\ell(|\mathbf{k}+\mathbf{K}|r_{MT}^{(t)})\,\dot{u}_\ell^{(t)}(r_{MT}^{(t)},E_l) - j_\ell(|\mathbf{k}+\mathbf{K}|r_{MT}^{(t)})\,\dot{u}_\ell^{\prime(t)}(r_{MT}^{(t)},E_l) \tag{3.26}$$

and

$$\beta_\ell^{(t)}(\mathbf{k}+\mathbf{K}) = j_\ell(|\mathbf{k}+\mathbf{K}|r_{MT}^{(t)})\,u_\ell^{\prime(t)}(r_{MT}^{(t)},E_l) - j'_\ell(|\mathbf{k}+\mathbf{K}|r_{MT}^{(t)})\,u_\ell^{(t)}(r_{MT}^{(t)},E_l)\,. \tag{3.27}$$

The radial functions $u_\ell(r)$ that occur in eqs. 3.24-3.27 are solutions of the ordinary differential equations (in atomic units)

$$\left[-\frac{d^2}{dr^2} + \frac{\ell(\ell+1)}{r^2} + V(r) - E_\ell\right] r u_\ell(r) = 0 \tag{3.28}$$

and

$$\left[-\frac{d^2}{dr^2} + \frac{\ell(\ell+1)}{r^2} + V(r) - E_\ell\right] r\dot{u}_\ell(r) = r u_\ell(r), \tag{3.29}$$

where $V(r)$ represents the spherical average of the crystsl potential within the muffin-tin sphere of the t^{th} atom. Combining the plane-wave formula (eq. 3.19) and the LAPW ansatz (eq. 3.20) yields

$$\begin{aligned} a_{n,\mathbf{k}}(\mathbf{G}) &= \frac{\sqrt{\Omega}}{\Omega_0} \sum_{\mathbf{K}} c_{n,\mathbf{k}}(\mathbf{K}) \sum_t \sum_\alpha \Bigg\{ \int_{\Omega_0} d^3r \, \mathrm{e}^{-i(\mathbf{k}+\mathbf{G})\cdot\mathbf{r}} \\ &\times \sum_\ell \sum_m \Big[A^{t,\alpha}_{\ell,m}(\mathbf{k}+\mathbf{K}) \, u^{(t)}_\ell(|\mathbf{r}-\mathbf{r}_{t,\alpha}|, E_\ell) + B^{t,\alpha}_{\ell,m}(\mathbf{k}+\mathbf{K}) \, \dot{u}^{(t)}_\ell(|\mathbf{r}-\mathbf{r}_{t,\alpha}|, E_\ell) \Big] \\ &\times Y_{\ell,m}(\mathbf{r}-\mathbf{r}_{t,\alpha}) \, \Theta(r^{(t)}_{MT} - |\mathbf{r}-\mathbf{r}_{t,\alpha}|) + \frac{1}{\sqrt{\Omega}} \int_{\Omega_{int}} d^3r \, \mathrm{e}^{i(\mathbf{K}-\mathbf{G})\cdot\mathbf{r}} \Bigg\} , \end{aligned}$$

where Ω_{int} denotes the volume of the interstitial region between all muffin-tin spheres in the crystal. After evaluation of the Heaviside function Θ, inserting the identity

$$\mathrm{e}^{-i(\mathbf{k}+\mathbf{G})\cdot\mathbf{r}} = 4\pi \sum_{\ell'} \sum_{m'} (-i)^{\ell'} \, j_{\ell'}(|\mathbf{k}+\mathbf{G}|r) \, Y_{\ell',m'}(\mathbf{k}+\mathbf{G}) \, Y^*_{\ell',m'}(\mathbf{r})$$

with $j_\ell(x)$ and $Y_{\ell,m}$ being the spherical Bessel functions and the spherical harmonics, and further applying some elementary but tedious mathematics the plane-wave fromula can be rewritten as

$$\begin{aligned} a_{n,\mathbf{k}}(\mathbf{G}) &= \frac{4\pi\sqrt{\Omega}}{\Omega_0} \sum_{\mathbf{K}} c_{n,\mathbf{k}}(\mathbf{K}) \Bigg\{ \sum_t \sum_\alpha \mathrm{e}^{-i(\mathbf{k}+\mathbf{G})\cdot\mathbf{r}_{t,\alpha}} \sum_{\ell,m} \sum_{\ell',m'} (-i)^{\ell'} \int_{r=0}^{r^{(t)}_{MT}} dr \, r^2 \, j_{\ell'}(|\mathbf{k}+\mathbf{G}|r) \\ &\times \Big[A^{t,\alpha}_{\ell,m}(\mathbf{k}+\mathbf{K}) \, u^{(t)}_\ell(r, E_\ell) + B^{t,\alpha}_{\ell,m}(\mathbf{k}+\mathbf{K}) \, \dot{u}^{(t)}_\ell(r, E_\ell) \Big] \, Y_{\ell',m'}(\mathbf{k}+\mathbf{G}) \\ &\times \int dw \, Y^*_{\ell',m'}(\mathbf{r}) Y_{\ell,m}(\mathbf{r}) + \frac{1}{\sqrt{\Omega}} \int_{\Omega_{int}} d^3r \, \mathrm{e}^{i(\mathbf{K}-\mathbf{G})\cdot\mathbf{r}} \Bigg\} . \end{aligned}$$

This expression can further be reduced by implementing the orthonormalization rule

$$\int dw \, Y^*_{\ell',m'}(\mathbf{r}) \, Y_{\ell,m}(\mathbf{r}) = \delta_{\ell,\ell'} \, \delta_{m,m'}$$

to

$$\begin{aligned}
a_{n,\mathbf{k}}(\mathbf{G}) &= \sum_{\mathbf{K}} c_{n,\mathbf{k}}(\mathbf{K}) \left\{ \sum_t \sum_\alpha \frac{(4\pi)^2\sqrt{\Omega}}{\Omega_0} \mathrm{e}^{-i(\mathbf{k}+\mathbf{G})\cdot\mathbf{r}_{t,\alpha}} \sum_{\ell,m} (-i)^\ell \, Y_{\ell,m}(\mathbf{k}+\mathbf{G}) \right. \\
&\times \int_{r=0}^{r_{MT}^{(t)}} dr\, r^2\, j_\ell(|\mathbf{k}+\mathbf{G}|r) \, \left[A_{\ell,m}^{t,\alpha}(\mathbf{k}+\mathbf{K})\, u_\ell^{(t)}(r,E_\ell) + B_{\ell,m}^{t,\alpha}(\mathbf{k}+\mathbf{K})\, \dot{u}_\ell^{(t)}(r,E_\ell) \right] \\
&+ \left. \frac{1}{\Omega_0} \int_{\Omega_{int}} d^3r\, \mathrm{e}^{i(\mathbf{K}-\mathbf{G})\cdot\mathbf{r}} \right\} . \qquad (3.30)
\end{aligned}$$

The next step is the separation of the last integral over the interstitial regions as

$$\int_{\Omega_{int}} d^3r\, \mathrm{e}^{i(\mathbf{K}-\mathbf{G})\cdot\mathbf{r}} = \int_{\Omega_0} d^3r\, \mathrm{e}^{i(\mathbf{K}-\mathbf{G})\cdot\mathbf{r}} - \int_{\Omega_{allMTs}} d^3r\, \mathrm{e}^{i(\mathbf{K}-\mathbf{G})\cdot\mathbf{r}} = \Omega_0\, \delta_{\mathbf{K},\mathbf{G}} - \int_{\Omega_{allMTs}} d^3r\, \mathrm{e}^{i(\mathbf{K}-\mathbf{G})\cdot\mathbf{r}},$$

where Ω_{allMTs} denotes the volume over all muffin-tin spheres within the unit cell Ω_0. The evaluation of this integral can be done analytically which leads to

$$\int_{\Omega_{allMTs}} d^3r\, \mathrm{e}^{i(\mathbf{K}-\mathbf{G})\cdot\mathbf{r}} = 4\pi \left(r_{MT}^{(t)}\right)^3 \mathrm{e}^{i(\mathbf{K}-\mathbf{G})\cdot\mathbf{r}_{t,\alpha}} \frac{j_1(|\mathbf{K}-\mathbf{G}|r_{MT}^{(t)})}{|\mathbf{K}-\mathbf{G}|r_{MT}^{(t)}} .$$

Including equations 3.24 and 3.25 into equation 3.30 yields

$$\begin{aligned}
a_{n,\mathbf{k}}(\mathbf{G}) &= c_{n,\mathbf{k}}(\mathbf{G}) + \sum_{\mathbf{K}} c_{n,\mathbf{k}}(\mathbf{K}) \sum_t \frac{4\pi\left(r_{MT}^{(t)}\right)^2}{\Omega_0} \sum_\alpha \mathrm{e}^{i(\mathbf{K}-\mathbf{G})\cdot\mathbf{r}_{t,\alpha}} \\
&\times \left\{ 4\pi \sum_\ell \left(\sum_m Y_{\ell,m}(\mathbf{k}+\mathbf{G}) Y_{\ell,m}^*(\mathbf{k}+\mathbf{K}) \right) \int_{r=0}^{r_{MT}^{(t)}} dr\, r^2\, j_\ell(|\mathbf{k}+\mathbf{G}|r) \right. \\
&\times \left[\alpha_\ell^{(t)}(\mathbf{k}+\mathbf{K})\, u_\ell^{(t)}(r,E_\ell) + \beta_\ell^{(t)}(\mathbf{k}+\mathbf{K})\, \dot{u}_\ell^{(t)}(r,E_\ell) \right] \\
&- \left. r_{MT}^{(t)} \frac{j_1(|\mathbf{K}-\mathbf{G}|r_{MT}^{(t)})}{|\mathbf{K}-\mathbf{G}|r_{MT}^{(t)}} \right\} . \qquad (3.31)
\end{aligned}$$

Finally, a further simplification of eq. 3.31 can be done by using the formula

$$\sum_m Y_{\ell,m}(\mathbf{k}+\mathbf{G}) Y_{\ell,m}^*(\mathbf{k}+\mathbf{K}) = \frac{2\ell+1}{4\pi} P_\ell \left[\cos(\angle\mathbf{G},\mathbf{K})\right]$$

with $P_\ell(x)$ being the Legendre polynomial of the order ℓ, which results in

$$\begin{aligned}
a_{n,\mathbf{k}}(\mathbf{G}) &= c_{n,\mathbf{k}}(\mathbf{G}) + \sum_{\mathbf{K}} c_{n,\mathbf{k}}(\mathbf{K}) \sum_t \frac{4\pi \left(r_{MT}^{(t)}\right)^2}{\Omega_0} \sum_\alpha \mathrm{e}^{i(\mathbf{K}-\mathbf{G})\cdot\mathbf{r}_{t,\alpha}} \\
&\times \left\{ \sum_\ell (2\ell+1)\, P_\ell\left[\cos(\angle \mathbf{G},\mathbf{K})\right] \int_{r=0}^{r_{MT}^{(t)}} dr\, r^2\, j_\ell(|\mathbf{k}+\mathbf{G}|r) \right. \\
&\times \left[\alpha_\ell^{(t)}(\mathbf{k}+\mathbf{K})\, u_\ell^{(t)}(r,E_\ell) + \beta_\ell^{(t)}(\mathbf{k}+\mathbf{K})\, \dot{u}_\ell^{(t)}(r,E_\ell) \right] \\
&- \left. r_{MT}^{(t)} \frac{j_1(|\mathbf{K}-\mathbf{G}|r_{MT}^{(t)})}{|\mathbf{K}-\mathbf{G}|r_{MT}^{(t)}} \right\} . \qquad (3.32)
\end{aligned}$$

Inclusion of the positron ground state: In this section the specification of equation 3.32 for the pure positron wave function

$$\psi_+(\mathbf{r}) = \frac{1}{\sqrt{\Omega}} \sum_{\mathbf{G}} b_+(\mathbf{G})\, \mathrm{e}^{i\mathbf{G}\cdot\mathbf{r}} \qquad (3.33)$$

and for the enhanced positron wave function

$$\psi_+^{enh}(\mathbf{r}) = \sqrt{g(\mathbf{r})}\, \psi_+(\mathbf{r}) = \frac{1}{\sqrt{\Omega}} \sum_{\mathbf{G}} b_+^{enh}(\mathbf{G})\, \mathrm{e}^{i\mathbf{G}\cdot\mathbf{r}} \qquad (3.34)$$

will be derived. In case of the pure positron wave function that occurs in the independent particle approximation, only the electron quantities in eq. 3.32 need to be replaced by the corresponding positron quantities:

$$\begin{aligned}
b_+(\mathbf{G}) &= c_+(\mathbf{G}) + \sum_{\mathbf{K}} c_+(\mathbf{K}) \sum_t \frac{4\pi \left(r_{MT}^{(t)}\right)^2}{\Omega_0} \sum_\alpha \mathrm{e}^{i(\mathbf{K}-\mathbf{G})\cdot\mathbf{r}_{t,\alpha}} \\
&\times \left\{ \sum_\ell (2\ell+1)\, P_\ell\left[\cos(\angle \mathbf{G},\mathbf{K})\right] \int_{r=0}^{r_{MT}^{(t)}} dr\, r^2\, j_\ell(|\mathbf{G}|r) \right. \\
&\times \left[\alpha_\ell^{+(t)}(\mathbf{K})\, u_\ell^{+(t)}(r,E_\ell) + \beta_\ell^{+(t)}(\mathbf{K})\, \dot{u}_\ell^{+(t)}(r,E_\ell) \right] \\
&- \left. r_{MT}^{(t)} \frac{j_1(|\mathbf{K}-\mathbf{G}|r_{MT}^{(t)})}{|\mathbf{K}-\mathbf{G}|r_{MT}^{(t)}} \right\} . \qquad (3.35)
\end{aligned}$$

Concerning the plane-wave coefficients of the enhanced positron ground state, the situation can be considerably simplified by the use of a muffin-tin approximation for the enhancement function $g(\mathbf{r})$ as follows

$$g(\mathbf{r}) \approx \begin{cases} g^{(t)}(|\mathbf{r}|) & \text{for } \mathbf{r} \text{ in the } t^{th} \text{ MT sphere,} \\ g_{int} & \text{for } \mathbf{r} \text{ within the interstitial region.} \end{cases} \tag{3.36}$$

In this approximation the inclusion of the enhancement into equation 3.36 yields the following formula for the plane-wave coefficient of the enhanced positron ground state

$$\begin{aligned} b_+^{enh}(\mathbf{G}) &= c_+(\mathbf{G})\,\sqrt{g_{int}} + \sum_{\mathbf{K}} c_+(\mathbf{K}) \sum_t \frac{4\pi\left(r_{MT}^{(t)}\right)^2}{\Omega_0} \sum_\alpha \mathrm{e}^{i(\mathbf{K}-\mathbf{G})\cdot\mathbf{r}_{t,\alpha}} \\ &\times \left\{ \sum_\ell (2\ell+1)\,P_\ell\left[\cos(\angle\mathbf{G},\mathbf{K})\right] \int_{r=0}^{r_{MT}^{(t)}} dr\, r^2\, j_\ell(|\mathbf{G}|r)\sqrt{g^{(t)}(r)} \right. \\ &\times \left[\alpha_\ell^{+(t)}(\mathbf{K})\,u_\ell^{+(t)}(r,E_\ell) + \beta_\ell^{+(t)}(\mathbf{K})\,\dot{u}_\ell^{+(t)}(r,E_\ell)\right] \\ &- \left. r_{MT}^{(t)}\,\frac{j_1(|\mathbf{K}-\mathbf{G}|r_{MT}^{(t)})}{|\mathbf{K}-\mathbf{G}|r_{MT}^{(t)}}\,\sqrt{g_{int}} \right\}. \end{aligned} \tag{3.37}$$

3.4 Numerical evaluation of the EMD and EPMD in the plane-wave representation

After defining

$$\begin{aligned} p_x &= qe_y + e_{yz} r \cos\varphi \\ p_y &= qe_y - [e_x e_y r \cos\varphi - e_z r \sin\varphi]/e_{yz} \\ p_z &= qe_z - [e_x e_z r \cos\varphi + e_y r \sin\varphi]/e_{yz} \end{aligned} \tag{3.38}$$

and $e_{yz} = \sqrt{e_y^2 + e_z^2}$ eq. 2.1 can be written as

$$J(q, \mathbf{e}) = \int_{r=0}^{\infty} \int_{\varphi=0}^{2\pi} dr r d\varphi \rho(\mathbf{p}). \tag{3.39}$$

In order to calculate a Compton or Doppler profile, one has to know the EMD or EPMD at any point of the $\mathbf{p}$ space, which would require the knowledge of all energy eigenvalues and of the corresponding plane-wave coefficients for all occupied electron states $\mid n, \mathbf{k} >$ within the Brillouin zone. This, however, leads to an enormous numerical effort that can be reduced by using all symmetry properties of the crystal, especially concerning the point group operations. These operations are defined by a set of orthogonal matrices $\alpha_t, t = 1, \ldots, t_{max}$. The following relations are valid [20]:

$$\epsilon_{n,\alpha_t^{-1}\mathbf{K}} = \epsilon_{n,\mathbf{k}} \tag{3.40}$$

and

$$a^{PW}_{n,\alpha_t^{-1}\mathbf{k}}(\mathbf{K}) = \mathrm{e}^{-i\mathbf{K}\cdot\mathbf{s}_t} a^{PW}_{n,\mathbf{k}}(\alpha_t \mathbf{K}) \text{ and } a^{ep}_{n,\alpha_t^{-1}\mathbf{k}}(\mathbf{K}) = \mathrm{e}^{-i\mathbf{K}\cdot\mathbf{s}_t} a^{ep}_{n,\mathbf{k}}(\alpha_t \mathbf{K}), \tag{3.41}$$

where $\mathbf{s}_t$ means the non-trivial translation vector corresponding to the point group element α_t. Evaluation of Kronecker's delta $\delta_{\mathbf{k},\mathbf{p}-\mathbf{K}}$ in eq. 3.2 yields the following rule: *For each fixed vector* $\mathbf{p}$, *there is one and only one reciprocal-lattice vector* $\mathbf{K}(\mathbf{p})$ *that reduces* $\mathbf{p}$ *into the first BZ* [20]. Further one can rotate the vector $\mathbf{p} - \mathbf{K}(\mathbf{p})$ into the irreducible wedge (IW) of the Brillouin zone by the point group element called α_{IW}:

$$\mathbf{k}_{IW} = \alpha_{IW}[\mathbf{p} - \mathbf{K}(\mathbf{p})] \in IW. \tag{3.42}$$

Band structure calculations are now performed inside the irreducible wedge for a sample of $\mathbf{k}$ points which define a number of tetrahedrons which completely fill the irreducible wedge. For any vector $\mathbf{k}_{IW}$ obtained by eq. 3.42 it has then to be checked to which tetrahedron $\mathbf{k}_{IW}$ belongs. The corresponding Bloch energies and plane-wave coefficients are finally determined by linear interpolations within the tetrahedron. With this manipulations the one-dimensional Compton and Doppler profiles can now be obtained by numerical evaluation of

$$J^{Compton}(q,\mathbf{e}) = \frac{2\Omega_0}{(2\pi)^3} \int_{r=0}^{\infty} \int_{\varphi=0}^{2\pi} drrd\varphi \sum_n \Theta(\epsilon_F - \epsilon_{n,\mathbf{k}_{IW}}) \mid a^{PW}_{n,\mathbf{k}_I W}(\alpha_{IW}\mathbf{K}(\mathbf{p})) \mid^2 \quad (3.43)$$

and

$$J^{Doppler}(q,\mathbf{e}) = \frac{2\Omega_0}{(2\pi)^3} \int_{r=0}^{\infty} \int_{\varphi=0}^{2\pi} drrd\varphi \sum_n \Theta(\epsilon_F - \epsilon_{n,\mathbf{k}_{IW}}) \mid a^{ep}_{n,\mathbf{k}_I W}(\alpha_{IW}\mathbf{K}(\mathbf{p})) \mid^2 . \quad (3.44)$$

The integration of eqs. 3.43 and 3.44 now was performed by a two-dimensional Simpson integration as it is done in the program *comprof_10VAR.exe* [13]. The corresponding tetrahedrons are defined using the *SETK*-programs [25]. The number of data points and tetrahedrons varies for different structures of the unit cell (tab. 3.1):

Table 3.1: Number of data points and tetrahedrons defined by these points for the different unit cells used in section 4.1.

Structure	Number of data points	Number of tetrahedrons
body centered cubic	91	250
face centered cubic	89	250
simple cubic	84	216
simple tetragonal	90	240

4 Numerical Results

4.1 Investigation of FeCu alloys

4.1.1 Paramagnetic treatment

Investigated structures: Two series have been taken into account, one is based on the face-centered-cubic lattice as for pure copper, with a lattice constant of $d = 6.82$ a.u.. The other series is based on the real body-centered-cubic iron lattice ($d = 5.42$ a.u.). The alloys are assumed to appear in highly ordered and symmetric structure, hence, the composition of Fe and Cu atoms was not chosen to be randomly in the crystal. Further, for each series, five different concentrations of the Fe-atoms in the crystal ($x = 0, 25, 50, 75, 100$) have been investigated. The structures that have been used in particular are given in Tab. 4.1 and 4.2.

Table 4.1: Structures investigated for the fcc series of FeCu alloys. The lattice constant d has been chosen identical to that of the fcc Cu lattice ($d = 6.82$a.u.) as suggested in [26].

Composition	Space group	Number	Lattice constant
$Fe_{100}Cu_0$	Fm-3m	225	$a = d$
$Fe_{75}Cu_{25}$	Pm-3m	221	$a = d$
$Fe_{50}Cu_{50}$	P4/mmm	123	$a = b = \frac{d}{\sqrt{2}}$
$Fe_{25}Cu_{75}$	Pm-3m	221	$a = d$
Fe_0Cu_{100}	Fm-3m	225	$a = d$

The coordinates of the atomic arrangements have been obtained from Ref. [27]. In order to achieve good results the muffin-tin radius r_{MT} in the full-potential LAPW-calculations performed by the program WIEN2k has been chosen such that $2r_{MT} = d_{NN}$ for each arrangement, where d_{NN} means the nearest-neighbour-distance in the crystal lattice. Further, the energy to separate core states and valence states has been chosen

Table 4.2: Structures investigated for the bcc series of FeCu alloys. The lattice constant d has been chosen identical to that of the bcc Fe lattice (d = 5.42a.u.) as suggested in [26]. For bcc $Fe_{50}Cu_{50}$ two different atom arrangements were taken into consideration.

Composition	Space group	Number	Lattice constant
$Fe_{100}Cu_0$	Im-3m	229	$a = d$
$Fe_{75}Cu_{25}$	Fm-3m	225*	$a = 2d$
$Fe_{50}Cu_{50}$	Pm-3m	221	$a = d$
$Fe_{50}Cu_{50}$	Fd-3m	227	$a = 2d$
$Fe_{25}Cu_{75}$	Fm-3m	225*	$a = 2d$
Fe_0Cu_{100}	Im-3m	229	$a = d$

such, that the electronic states up to the 2p state are treated as core states, all other states (semi-core and valence states) are treated as valence states, hence for Fe

$$\underbrace{\mathrm{1s^2 2s^2 2p^6}}_{\text{core}}\ \underbrace{\mathrm{3s^2 3p^6}}_{\text{semi-core}}\ \underbrace{\mathrm{3d^6 4s^2}}_{\text{valence}}$$

and for Cu

$$\underbrace{\mathrm{1s^2 2s^2 2p^6}}_{\text{core}}\ \underbrace{\mathrm{3s^2 3p^6}}_{\text{semi-core}}\ \underbrace{\mathrm{3d^{10} 4s^1}}_{\text{valence}}.$$

This requires a separation energy of -7.0 Ry for bcc $Fe_{100}Cu_0$ and fcc $Fe_{100}Cu_0$ and -9.0 Ry for all other arrangements including Cu. The band structure calculations have been performed for the paramagnetic case, and no relativistic effects have been taken into account. In order to compare the results of the LAPW-calculation with former calculations in literature the density of states has been calculated for the considered alloys (figs. 4.1 and 4.2). The results agree quite well with those in Ref. [26].

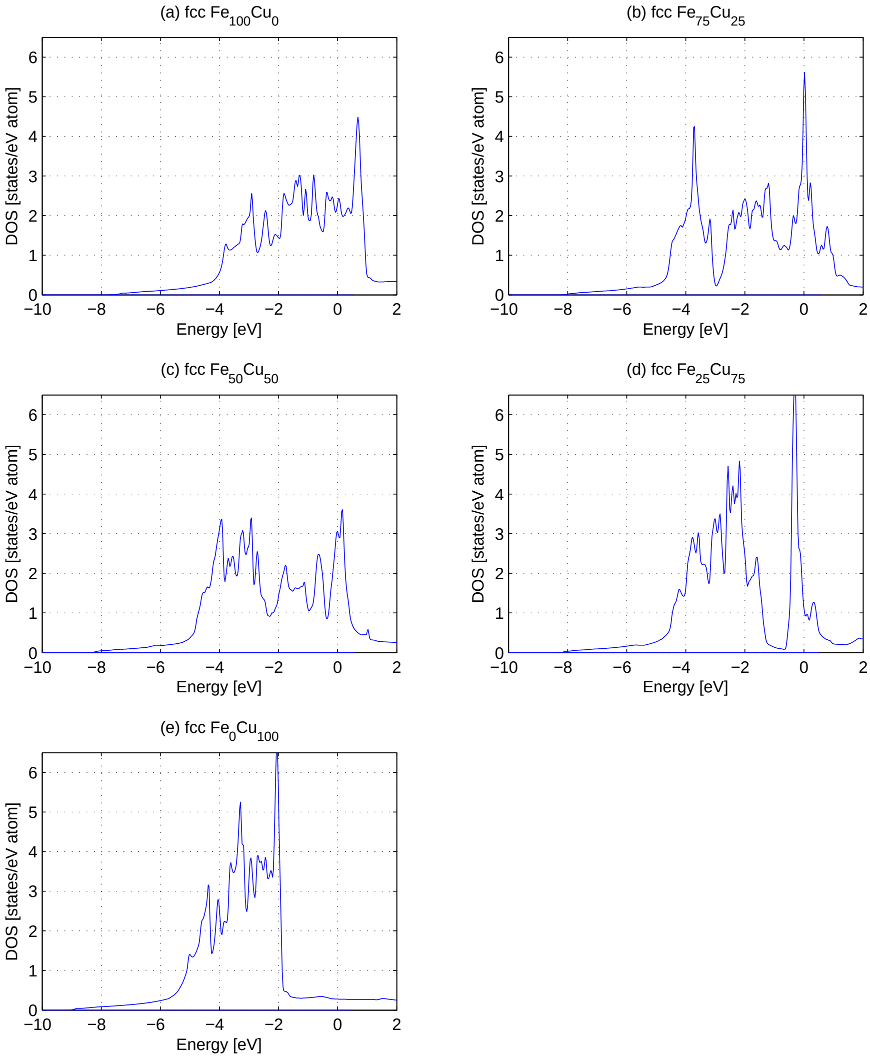

Figure 4.1: Nonpolarized density of states (DOS) for fcc Fe$_x$Cu$_{100-x}$ alloys for $x = 0$ (a), 25 (b), 50 (c), 75 (d) and 100 (e). The zero-energy represents the Fermi level.

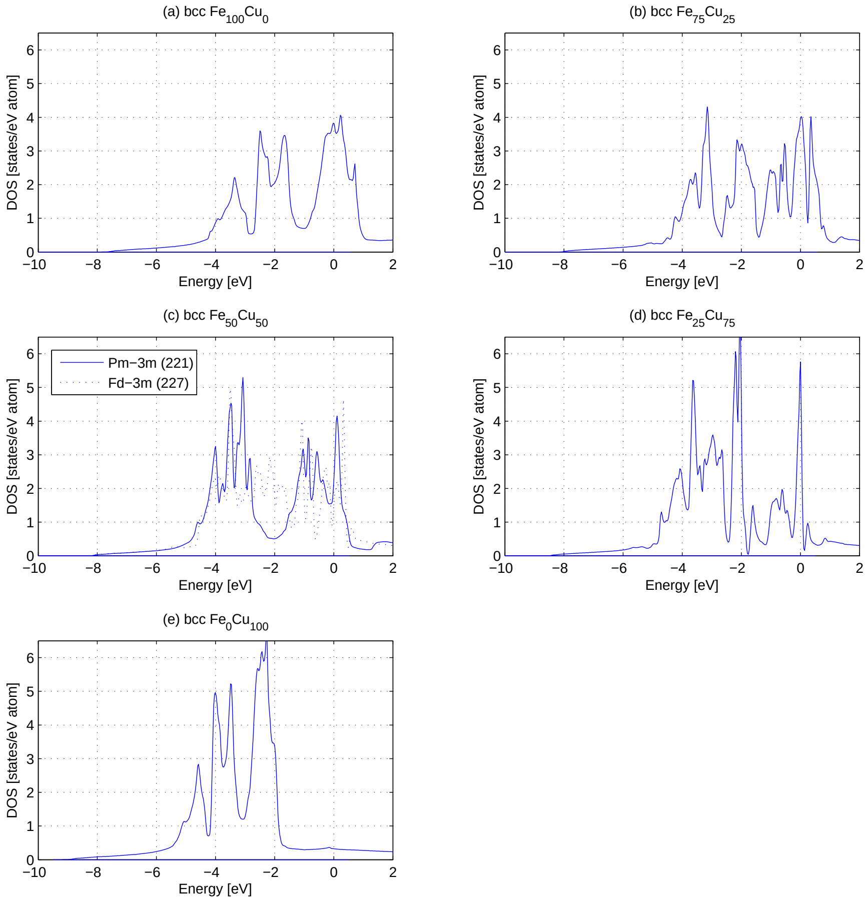

Figure 4.2: Nonpolarized density of states (DOS) for bcc Fe_xCu_{100-x} alloys for $x = 0$ (a), 25 (b), 50 (c), 75 (d) and 100 (e). The zero-energy represents the Fermi level.

Compton profiles: In order to evaluate the quality of a one-dimensional Compton profile calculated by the program *comprof_10VAR.exe* [13], the correlation between the number of coefficients used in the plane-wave representation for the electron Bloch functions (eq. 3.1) and the convergence of the profile has been investigated. The goal was to get a reliable calculation of Compton profiles within a momentum region up to approximately 50 mrad. This inclusion of the high-momentum region is of great importance since many experimental investigations using Compton or Doppler spectroscopy are done with special emphasis on this region. To study the convergence within this high-momentum region, it is convenient to use semilogarithmic diagrams, since the Compton profiles reach rather small values in this region. As one would expect, the number of plane-waves required to achieve this accuracy depends on the complexity of the investigated structure. To demonstrate this, the one-dimensional Compton profiles for the fcc copper crystal (1 atom per unit cell) has been calculated for various numbers of plane-waves (fig. 4.3). The same has been done for the bcc $Fe_{25}Cu_{75}$ alloy (in the Fm-3m structure, as given in tab. 4.2; 1 Fe and 3 Cu atoms per unit cell), which is one of the most complex structures among the considered FeCu alloys. The result is shown in fig. 4.4. For the simple 1-atomic fcc copper the desired convergence up to 50 mrad is already reached at a number of about 2000 plane-waves used for the plane wave representation of the electronic Bloch function (fig. 4.3). For the more complex bcc $Fe_{25}Cu_{75}$ alloy, however, approximately 6000 plane-waves are necessary to obtain similar accuracy (fig. 4.4). Thus, the more complicated the structure is, the more numerical effort is needed in order to achieve good results. Further, the effort grows with the region of momentum to be investigated, e.g up to 30 mrad no more than 3000 plane-waves are required for good convergence in the 4-atomic structure.

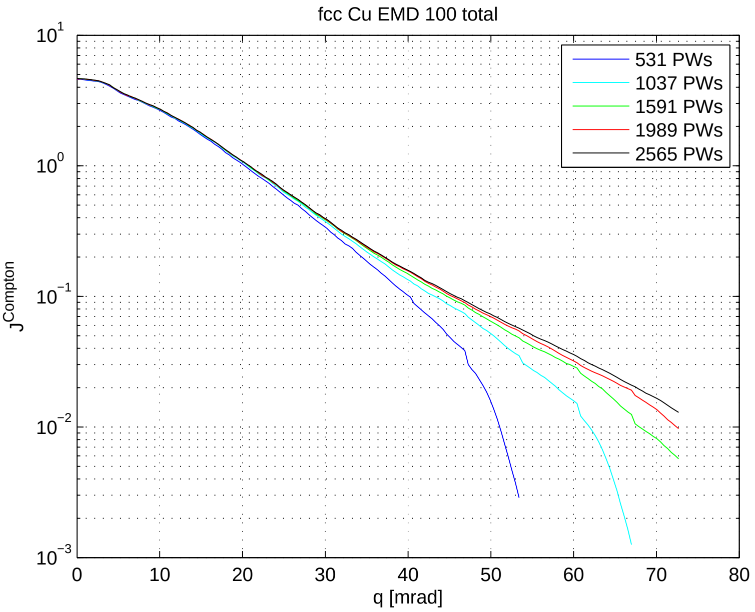

Figure 4.3: One-dimensional Compton profile for fcc Cu along the [100]-direction. All semi-core and valence electrons have been considered for various numbers of plane-wave coefficients from about 500 up to 2500. The desired convergence up to approximately 50 mrad is reached at about 2000 plane-waves.

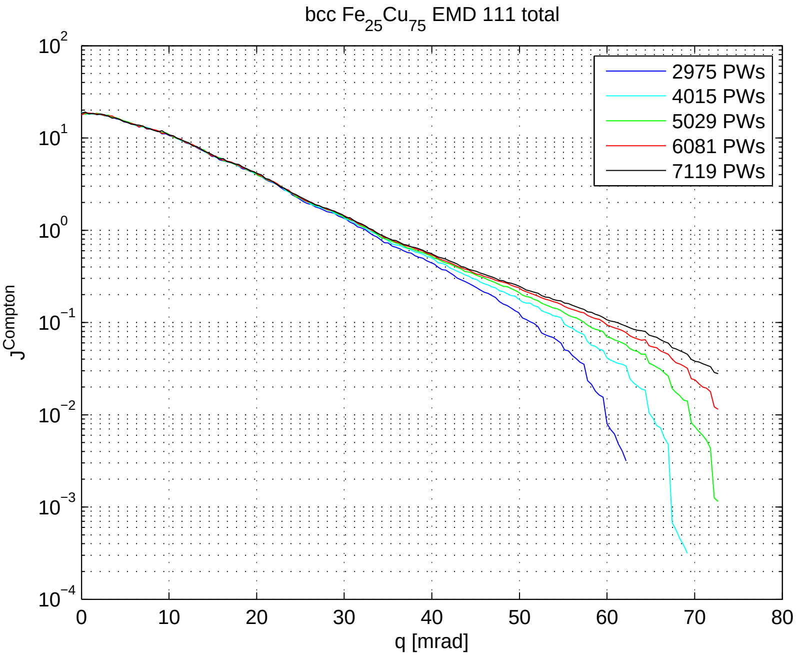

Figure 4.4: One-dimensional Compton profile for bcc $Fe_{25}Cu_{75}$ along the [111]-direction. All semi-core and valence electrons have been considered for various numbers of plane-wave coefficients from about 3000 up to 7000. The desired convergence up to approximately 50 mrad is finally reached at about 6000 plane-waves.

Semilogarithmic diagrams as they are used in figs. 4.3 and 4.4 can also be used to show how different electron bands contribute to the total Compton profile. This has been done for bcc Cu in fig. 4.5, where the Compton distributions of the 3s-, 3p- and the valence electrons (3d and 4s) are separately shown. An equivalent investigation for bcc $Fe_{25}Cu_{75}$ is presented in fig. 4.6. In this case one has to distinguish between the 3s and 3p contributions for Fe and Cu atoms. The contributions of the valence states of the different atoms, however, cannot be separated because the corresponding bands are completely mixed due to their high dispersion and the fact that their energy levels are quite close to each other.

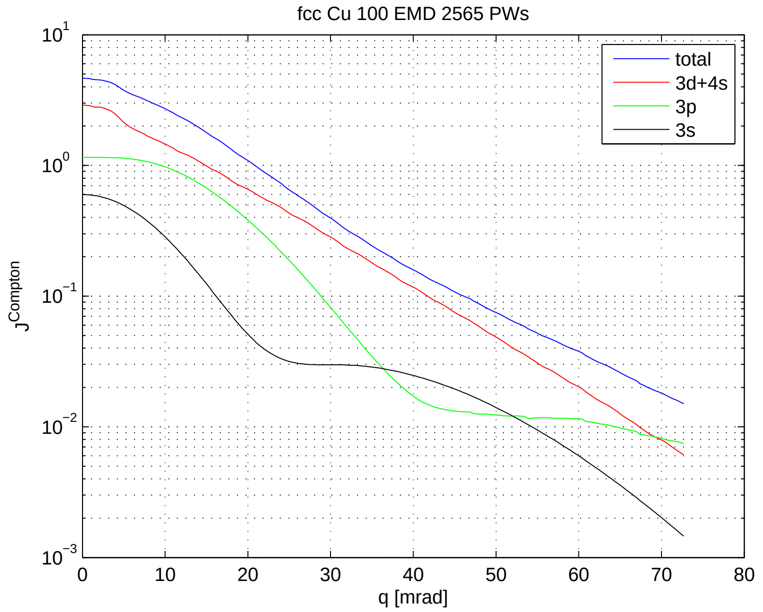

Figure 4.5: One-dimensional Compton profile for fcc Cu along the [100]-direction for different bands. The valence states (3d and 4s) can not be separated.

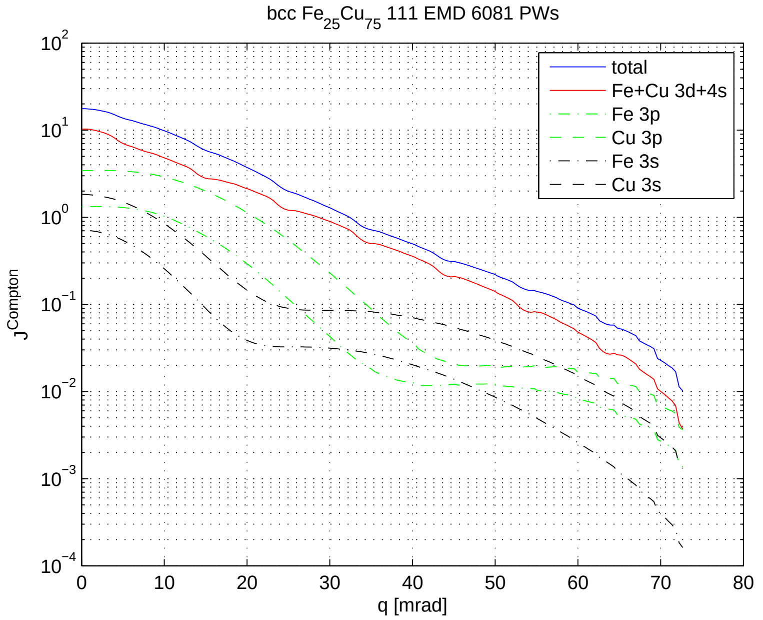

Figure 4.6: One-dimensional Compton profile for bcc $Fe_{25}Cu_{75}$ along the [111]-direction for different bands. The valence states (3d and 4s) can not be separated.

The separate presentation of contributions to the Compton profile due to different bands (figs. 4.5 and 4.6) shows, that the contribution of the semi-core states (3s and 3p) to the total profile is rather large in a momentum region from zero to about 20 mrad (3p) and then starts to increase again at about 25 mrad (3s), respectively 40 mrad (3p) towards the high-momentum region. One can also observe that the contributions of the semi-core states for Fe and Cu to the total profile in fig. 4.6 have almost the same shape in the semilogarithmic diagram. Further they have almost the same value per atom (note that in fig. 4.6 the contribution of the Cu states is counted three times due to the material's structure). Hence, any differences in shape of the one-dimensional Compton profiles, that may occur by variation of the fractions of iron and copper, arise from the contribution of the valence states (3d and 4s). This topic will be discussed later in this chapter.

Another quantity to determine the reliability of calculated one-dimensional Compton profiles is the number of electrons in the unit cell which should equal the area under the Compton profile as given in eq. 2.3. The result of this integration for the profiles of the bcc series of FeCu alloys along the [100]-direction (fig. 4.7) is given in tab. 4.3. The results of the integration agree quite well with the number of electrons, the relative error is around 1.5% – 3%.

Table 4.3: Number of electrons γ in all semi-core and valence states and integrated area of the one-dimensional Compton profile γ_{calc} for the bcc series of FeCu alloys along the [100]-direction.

Composition	γ	γ_{calc}
$Fe_{100}Cu_0$	16	15.71
$Fe_{75}Cu_{25}$	67	65.19
$Fe_{50}Cu_{50}$	35	34.38
$Fe_{50}Cu_{50}$	70	67.94
$Fe_{25}Cu_{75}$	73	70.80
Fe_0Cu_{100}	19	18.48

In the following, the Compton profiles of the two series proposed in [26] are shown. The calculations have been performed for the [100]- and the [110]-direction of the crystal lattices. In case of the fcc $Fe_{50}Cu_{50}$ alloy (see tab. 4.1), the so called CuAu-structure [27], the unit cell is a tetragonal structure where the primitive vectors in the base plane

($k_z = 0$) are rotated by 45^0 with respect to the primitive vectors of the cubic structures. Elementary considerations reveal that the [100]-direction of the cubic lattice is equal to the [110]-direction in the tetragonal lattice, the cubic [110]-direction corresponds to the [010]-direction in the tetragonal case. 7000 plane-waves have been used for the calculations, all semi-core and valence electrons have been considered. The results are shown in figs. 4.7 - 4.10.

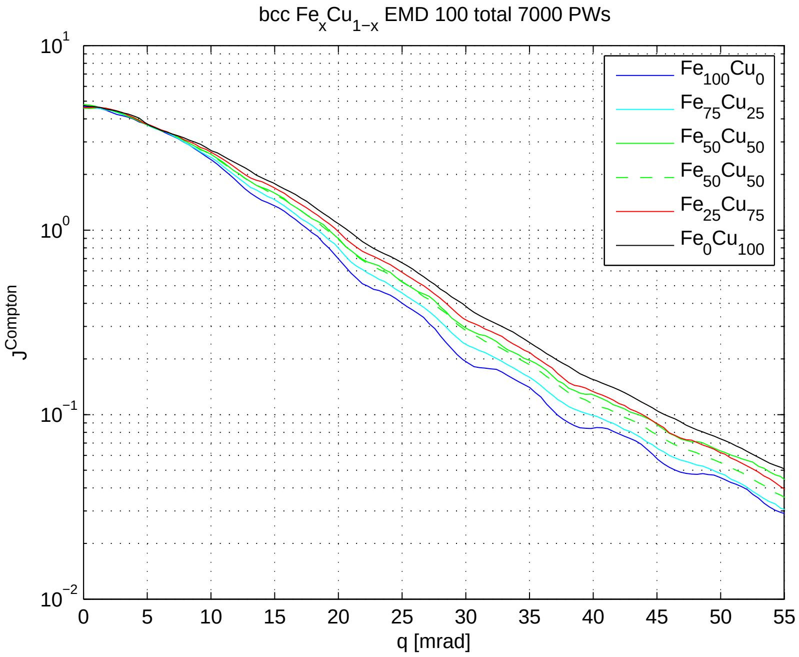

Figure 4.7: 1D-Compton profiles for bcc Fe$_x$Cu$_{1-x}$ alloys along the [100]-direction.

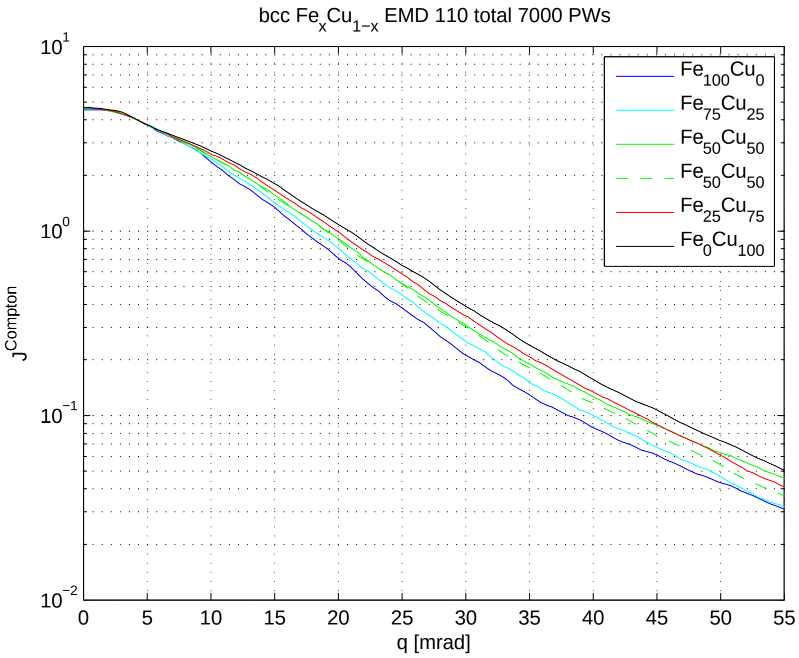

Figure 4.8: 1D-Compton profiles for bcc Fe$_x$Cu$_{1-x}$ alloys along the [110]-direction.

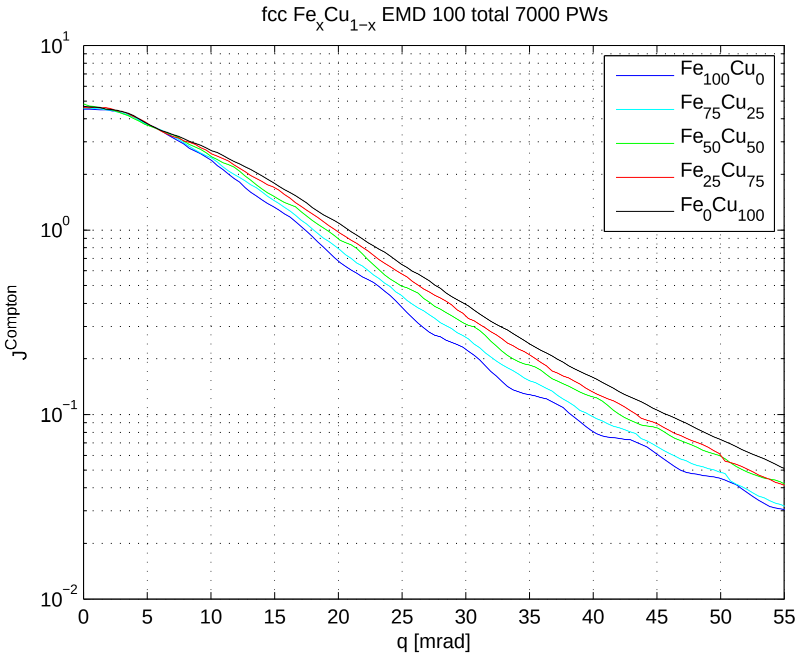

Figure 4.9: 1D-Compton profiles for fcc Fe$_x$Cu$_{1-x}$ alloys along the [100]-direction.

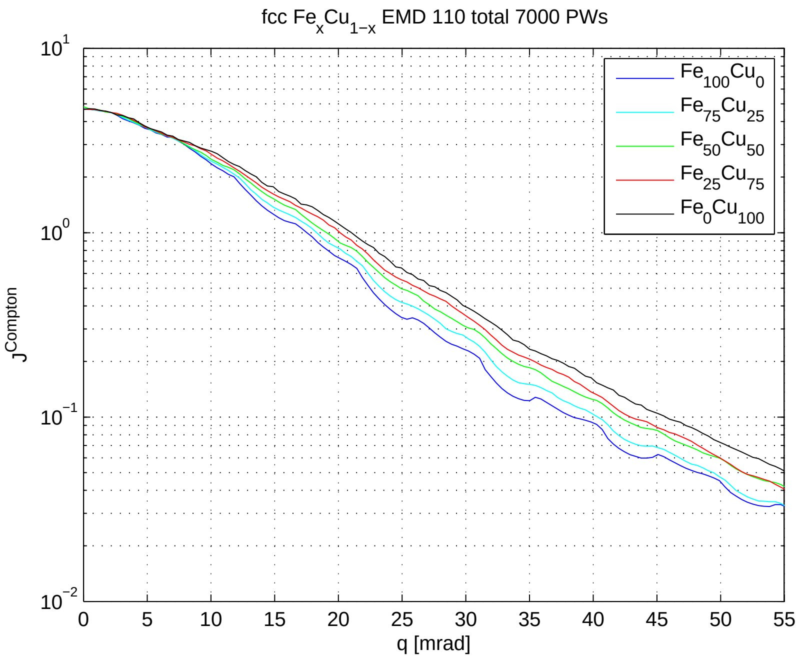

Figure 4.10: 1D-Compton profiles for fcc Fe$_x$Cu$_{1-x}$ alloys along the [110]-direction.

The semilogarithmic diagrams in figs. 4.7 - 4.10 predominantly show the behaviour of the Compton profiles in the high-momentum region. In this regard, the following considerations are useful for their discussion. The electron momentum distribution in a crystal basically depends on the electron's spatial localization. Strongly bound electrons are highly localized, while weakly bond electrons are more delocalized in space. Regarding an electronic band structure one can assume that spatially sharply localized electrons correspond to bands having a small dispersion in momentum space and, hence, having a narrow bandwidth. Generally one can observe, that the localization of electrons in crystals grows as

- the electron energy, with respect to the Fermi level, decreases
- the azimuthal quantum number decreases.

Hence, one can assume that the semi-core states (3s and 3p) of iron and copper are strongly localized, since their energies are several Ry lower than the Fermi energy. The 3d bands are also strongly localized because they have a larger azimuthal quantum number, but since the energies of the Cu 3d bands are somewhat lower than in case of Fe, one can assume that the copper 3d electrons are more localized than the iron 3d electrons. According to the Heisenberg uncertainty principle, states that are strongly localized in real space are strongly delocalized in momentum space and vice versa. Delocalization in momentum space further means a higher contribution to the high-momentum region in the Compton profile. Hence, the weaker localization in real space of the Fe 3d states with respect to the Cu 3d states yields larger values of the Fe profiles in the high-momentum region as the fraction of Cu in the crystal increases. This can be observed in figs. 4.7 - 4.10.

The one-dimensional Compton profiles for Fe, fcc and bcc $Fe_{50}Cu_{50}$ are shown in fig. 4.11. The profiles have a Gaussian shape and for the fcc and bcc $Fe_{50}Cu_{50}$ they coincide, the profiles for pure Fe and pure Cu, however, have significant different shapes. While the Fe profile is rather sharp, with a high peak at $q = 0$, this peak is much lower in the Cu profile, but, as in the semilogarithmic diagram, there are larger values in the high-momentum region of the Cu profile.

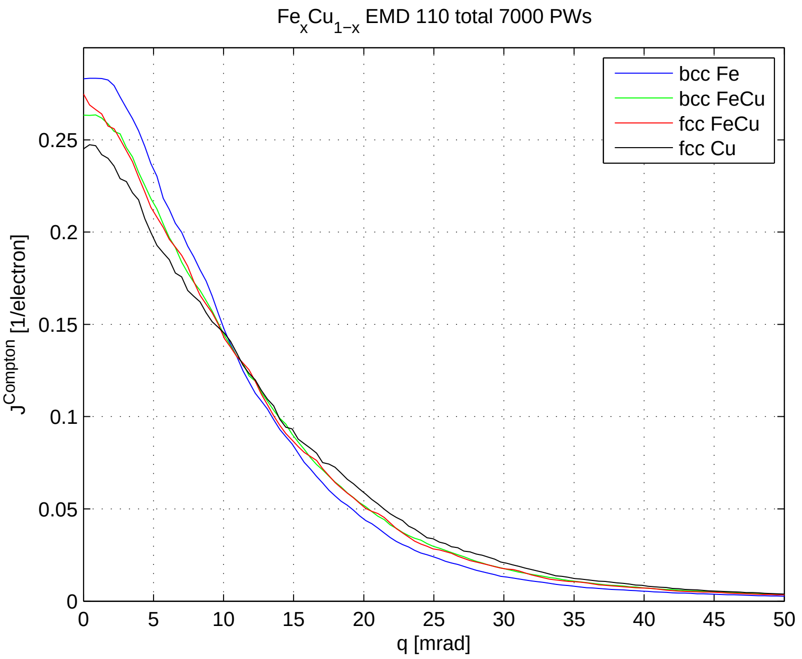

Figure 4.11: 1D-Compton profiles for $Fe_{100}Cu_0$, $Fe_{50}Cu_{50}$ and Fe_0Cu_{100} alloys along the [110]-direction. All curves are normalized to the same area.

4.1.2 Ferromagnetic calculations

Investigated structures: According to Ref. [7], the series shown in chapter 4.1.1 is somewhat artificial due to the following reasons:

- for all alloys containing Fe its ferromagnetism should be taken into account. This aspect will be treated in this chapter.
- as we learn from Ref. [7], the stability of the $\mathrm{Fe}_x\mathrm{Cu}_{1-x}$ might be quite different in their fcc or bcc realization.

It is no surprise that in case of dominating Fe, the bcc structure will be more stable while alloys with dominating Cu will preferably form a bcc structure. $\mathrm{Fe}_{1-x}\mathrm{Cu}_x$ alloys have a single bcc phase for $0 < x < 0.4$ and a single fcc phase for $0.6 < x < 1.0$, while both structures are likely to exist in the region of $0.4 < x < 0.6$ [7]. Further the lattice constants for the different compositions are modified according to the equilibrium lattice constants calculated using the generalized gradient approximation in Ref. [7]. Therefore only the structures as given in table 4.4 have been used for further calculations and the discussion starts again with the DOS of these materials.

Table 4.4: Crystal structures used for further calculations of the one-dimensional Compton profiles for $\mathrm{Fe}_{1-x}\mathrm{Cu}_x$ alloys, according to Ref. [7].

Composition	Structure	Space group	Lattice constant [A]
$\mathrm{Fe}_{100}\mathrm{Cu}_0$	bcc	Im-3m	2.843
$\mathrm{Fe}_{75}\mathrm{Cu}_{25}$	bcc	Fm-3m	2.888
$\mathrm{Fe}_{50}\mathrm{Cu}_{50}$	bcc	Pm-3m	2.900
$\mathrm{Fe}_{50}\mathrm{Cu}_{50}$	fcc	P/4mmm	3.637
$\mathrm{Fe}_{25}\mathrm{Cu}_{75}$	fcc	Pm-3m	3.631
$\mathrm{Fe}_0\mathrm{Cu}_{100}$	fcc	Fm-3m	3.616

For this reason, a more detailed presentation of the density of states has been chosen for the materials given in table 4.4. In fig. 4.12, the d-parts separated into their Cu (red line) and Fe (blue line) contributions are shown. It is not surprising that from pure Fe to pure Cu the density of states of the d electrons of copper is reduced continuously, but it is interesting to observe that this reduction takes place from the iron side of the spectrum. The remaining d contribution of the DOS for Cu is more and more shifted to smaller energies.

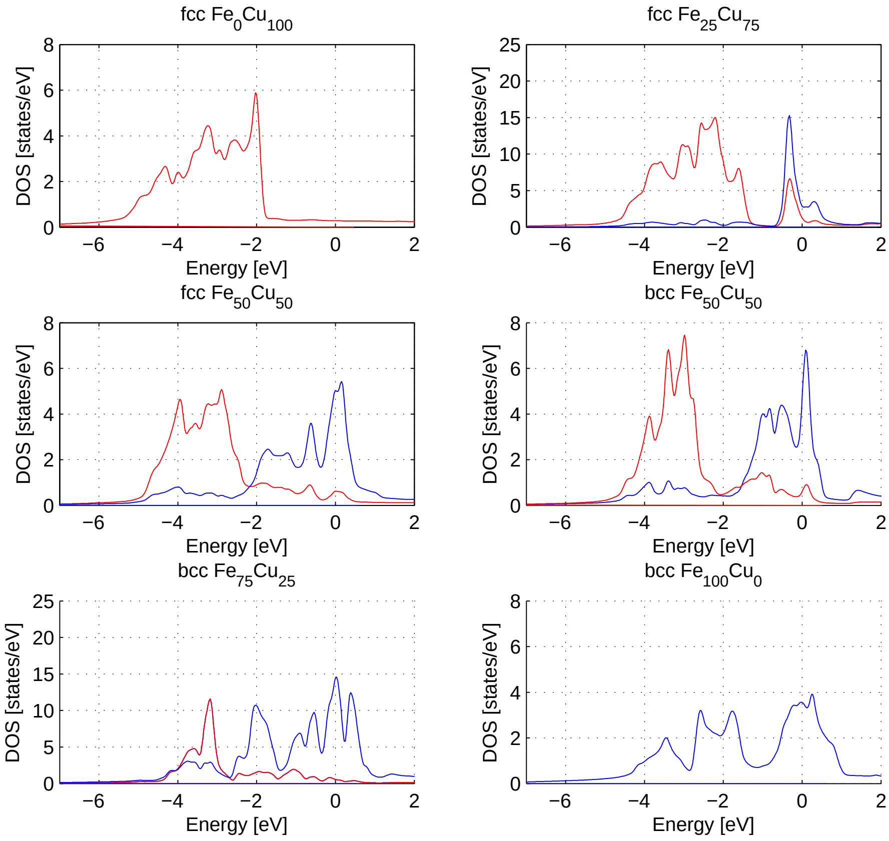

Figure 4.12: Nonpolarized density of states (DOS) for the d-parts of Fe$_x$Cu$_{100-x}$ alloys as given in table 4.4, separated into their Cu (red line) and Fe (blue line) contributions. The zero-energy represents the Fermi level.

Compton profiles: In the next step the one dimensional-Compton profiles for the Fe$_{1-x}$Cu$_x$ alloys as given in table 4.4 have been calculated again, but this time for all structures containing Fe spin-polarized LAPW calculations have been performed using *WIEN2k*. Again all semicore and valence states have been considered, 6800 plane waves have been used. In the ferromagnetic case the results consist of two one-dimensional Compton profiles, one for the spin up electrons and another one for the spin down electrons. Integration over the profiles again yields the number of electrons (eq. 2.3) that contribute to the associated profile, hence the number of electrons with spin up (γ_{up}) or spin down (γ_{dn}). The sum of the areas under the two profiles ($\gamma_{up} + \gamma_{dn}$) yields the total number of electrons in the considered semicore and valence states of the structure, and their difference ($\gamma_{up} - \gamma_{dn}$) describes the magnetic moment per unit cell in units of Bohr magnetons.

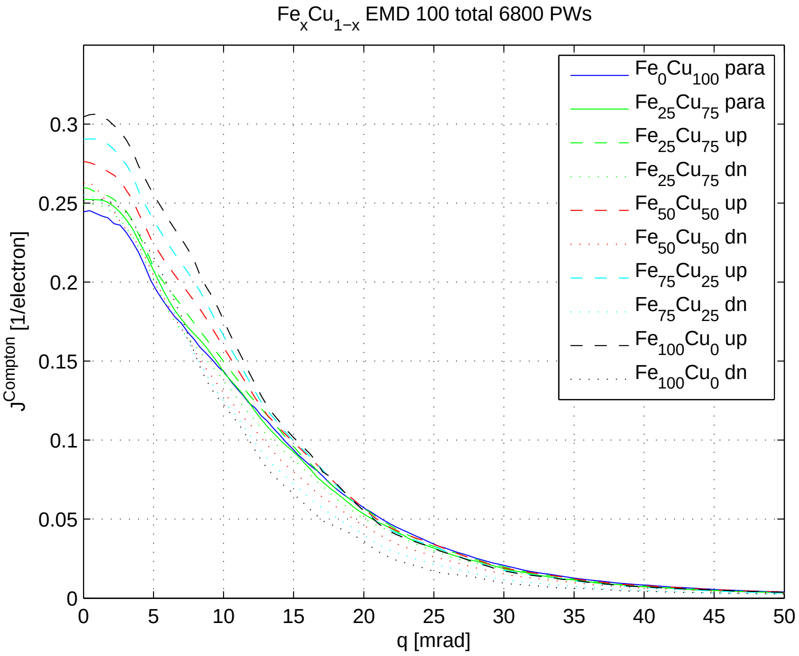

Figure 4.13: Normalized 1D-Compton profiles for ferromagnetic Fe$_{1-x}$Cu$_x$ alloys according to table (4.4) along the [100]-direction.

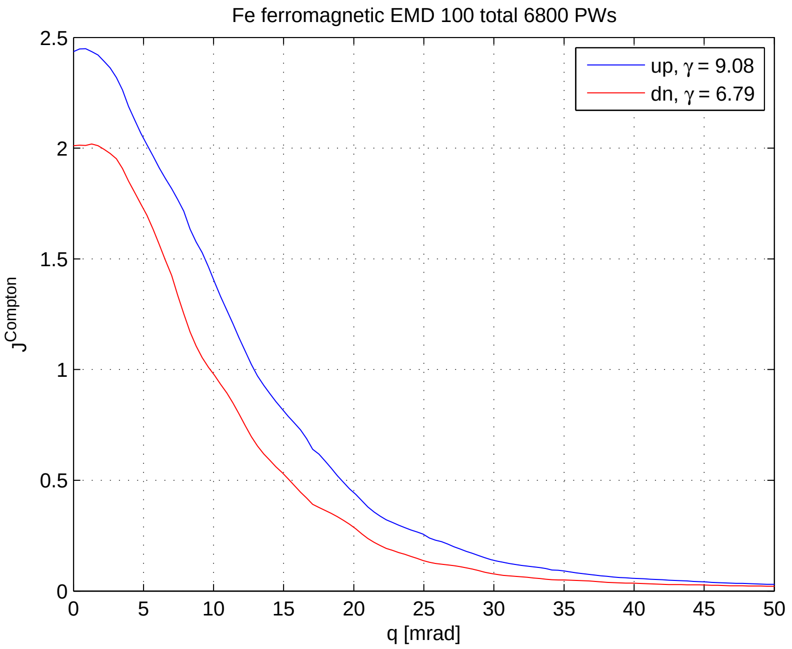

Figure 4.14: 1D-Compton profiles for ferromagnetic $Fe_{100}Cu_0$ along the [100]-direction.

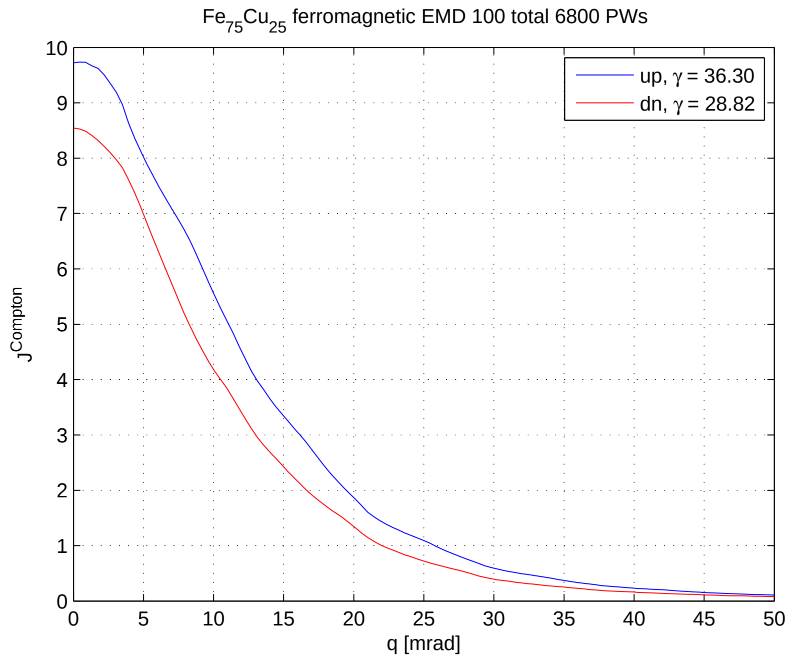

Figure 4.15: 1D-Compton profiles for ferromagnetic $Fe_{75}Cu_{25}$ along the [100]-direction.

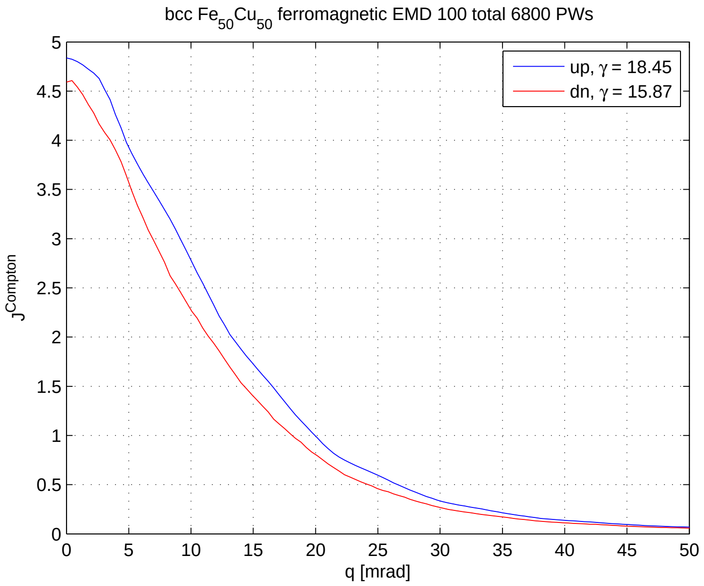

Figure 4.16: 1D-Compton profiles for ferromagnetic bcc $Fe_{50}Cu_{50}$ along the [100]-direction.

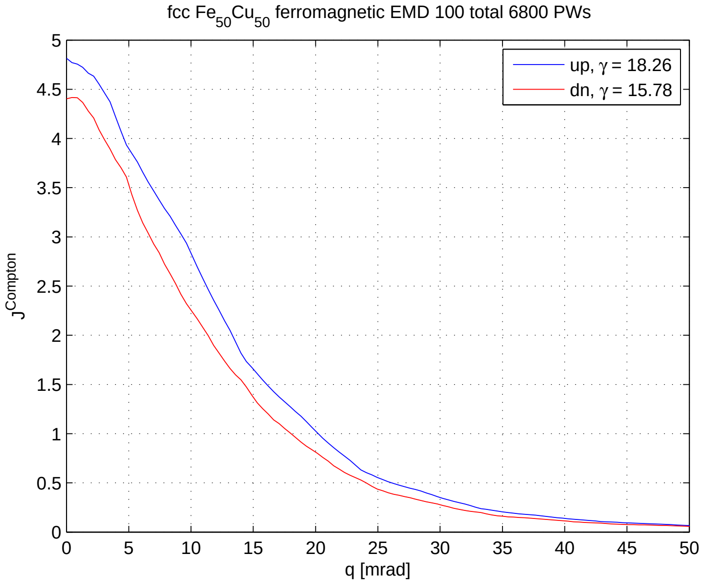

Figure 4.17: 1D-Compton profiles for ferromagnetic bcc $Fe_{50}Cu_{50}$ along the [100]-direction.

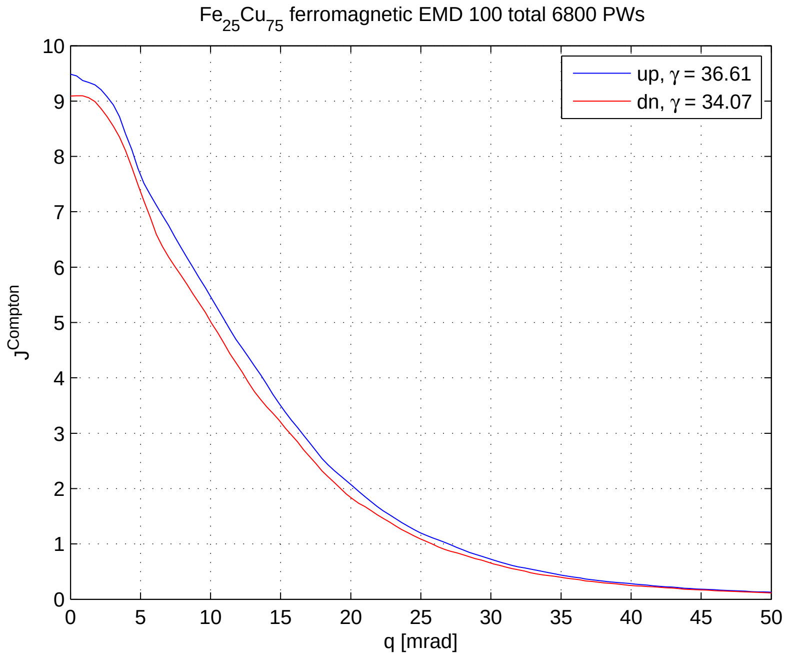

Figure 4.18: 1D-Compton profiles for ferromagnetic bcc $Fe_{25}Cu_{75}$ along the [100]-direction.

As a measure of quality for the ferromagnetic one-dimensional Compton profiles (fig. 4.13-4.18) the number of electrons in the semi-core and valence states obtained by integration of the profiles is given in table 4.5. Again the results of the integration agree quite well with the number of electrons, the relative error is less than 3.5% in each case.

Table 4.5: Integrated ferromagnetic one-dimensional Compton profiles compared to the number of electrons in semi-core and valence states.

Composition	γ_{up}	γ_{dn}	$\gamma_{calc} = \gamma_{up} + \gamma_{dn}$	γ
$Fe_{100}Cu_0$	9.08	6.74	15.82	16
$Fe_{75}Cu_{25}$	36.30	28.82	65.12	67
$Fe_{50}Cu_{50}$ bcc	18.45	15.87	34.32	35
$Fe_{50}Cu_{50}$ fcc	18.26	15.78	34.04	35
$Fe_{25}Cu_{75}$	36.61	34.07	70.68	73

Further the magnetic moment can be obtained from the ferromagnetic one-dimensional Compton profiles. It is simply given by

$$\mu = \gamma_{up} - \gamma_{dn}, \tag{4.1}$$

where μ is the magnetic moment per unit cell in units of the Bohr magneton μ_B. The magnetic moments for the investigated $\mathrm{Fe}_{1-x}\mathrm{Cu}_x$ alloys determined from the values in table 4.5 using equation 4.1 are shown in figure 4.19. As one would expect the averaged magnetic momentum per atom decreases almost linearly with the concentration x of Cu atoms in the crystal. The magnetic moment per Fe atom, however, increases as x grows. The reason is reduced symmetry on the one hand and the loss of magnetic neighbours as x increases on the other hand. These effects narrow the 3d bandwidth and thus lead to a larger density of states at the Fermi energy that increases the magnetic moment [7].

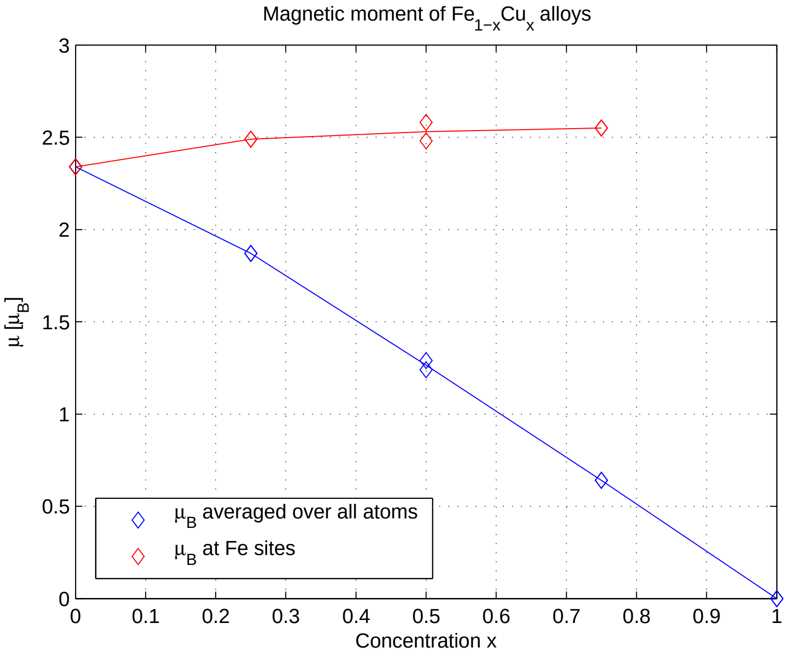

Figure 4.19: Magnetic moments of $\mathrm{Fe}_{1-x}\mathrm{Cu}_x$ determined from the one-dimensional Compton profiles. The blue graph represents the magnetic moment averaged over all atoms in the unit cell, the red one shows the magnetic moment at the Fe sites.

4.1.3 Doppler profiles

In this section, the Doppler profiles for the $Fe_{1-x}Cu_x$ alloys as given in table 4.4 are presented. The calculations have been performed for the independent particle model (eq. 2.8) as well as including the enhancement effect (see sec. 3.2). For the calculation of the Doppler profiles no ferromagnetic effects have been taken into account, neither for the electron states, nor for the positron ground state. As it is done for the Compton profiles (see sec. 4.1.1, figs. 4.3 and 4.4) the convergence of the Doppler profiles is first checked. For pure copper in the IPM, the results are shown in fig. 4.20. As in case of the Compton profiles mentioned above, the convergence in the high-momentum region first increases with the number of plane-wave coefficients. At a higher number of electron-positron Fourier coefficients used, the profile shows a crazy behaviour for $q > 35$ mrad. The reason for this can be found in eq. 3.5:

$$a^{ep}_{n,\mathbf{k}}(\mathbf{K}) := \sum_{\mathbf{G}} a^{PW}_{n,\mathbf{k}}(\mathbf{G}) b^{PW}_{+}(\mathbf{K}-\mathbf{G}).$$

According to the above equation, the electron-positron plane-wave coefficients $a^{ep}_{n,\mathbf{k}}$ for a reciprocal-lattice vector $\mathbf{K}$ are obtained by a convolution of the given set of electron plane-wave coefficients $a^{PW}_{n,\mathbf{k}}(\mathbf{G})$, $(\mathbf{G} = 1, \ldots, \mathbf{G}_{max})$ with the positron plane-wave coefficients b^{PW}_{+} centered at $\mathbf{K}$. A schematic presentation of this situation is given in fig. 4.21, left diagram. If, however, $\mathbf{K}$ gets too large and, hence, lies too near to $\mathbf{G}_{max}$, the convolution in the above formula gets defect, as it is shown in fig. 4.21, right diagram. This means, that, in case of a number of $\mathbf{G}_{max}$ electron plane-wave coefficients, reliable results for the electron-positron plane-wave coefficients $a^{ep}_{n,\mathbf{k}}(\mathbf{K})$ can only be obtained for approximately $K_{max} \leq \frac{G_{max}}{2}$. A feasible method to check the reliability of the electron-positron plane-wave coefficients $a^{ep}_{n,\mathbf{k}}(\mathbf{K})$ calculated using equation 3.5 is to analyse the Doppler profiles of the so-called semi-core bands (3s+3p). The Compton profiles of these bands are almost perfectly isotropic in momentum space. Further, this property must also be valid for the Doppler profiles of these bands, since the wave function of the positron being in ground state (1s-symmetry) does certainly not change this situation. Hence, all deviations of these Doppler profiles from isotropy in the q space indicate numerical problems concerning the determination of the electron-positron plane-wave coefficients. The results of this test for the $Fe_{25}Cu_{25}$ alloy, performed in three different directions in momentum space, are shown in figure 4.22. Regarding the right picture (5041 electron-positron plane-wave coefficients), the profiles along the different directions coincide up to about 45 mrad, then their behaviour becomes somewhat crazy due to the reason mentioned above. The use of lower numbers of electron-positron plane-wave coefficients, however, yields almost coincident Doppler profiles along the three different directions. Similar tests concerning the other investigated $Fe_{1-x}Cu_x$ alloys lead to the same results. Hence, for a number of 6800-6900 electron plane-wave coefficients (as used in this work), the highest convergence (up to more than 50 mrad for pure Fe and Cu, up to about 45 mrad for the structures of higher complexity) is obtained by using about 4000 electron-positron plane-wave coefficients. This rule is also valid in case of the enhanced positron, the local multiplicative enhancement factor (see sec. 3.2) does not alter the situation explained above.

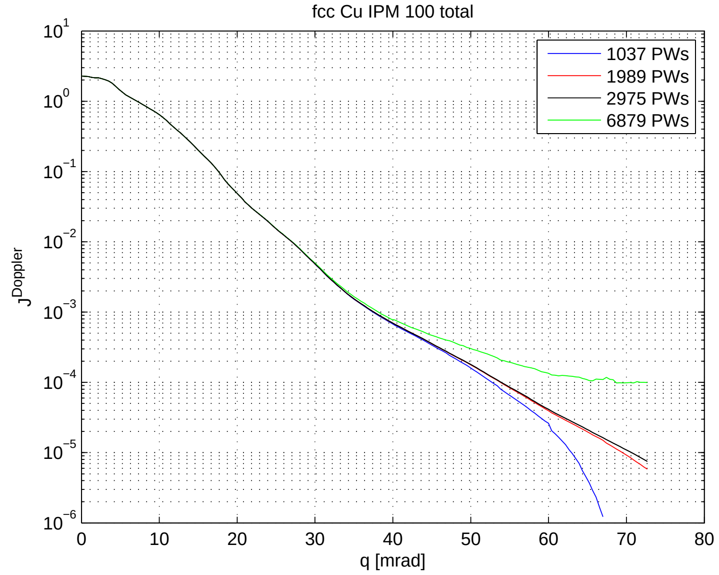

Figure 4.20: One-dimensional Doppler profiles for Cu along the [100]-direction according to the independent particle model and different numbers of electron-positron Fourier coefficients (eq. 3.5).

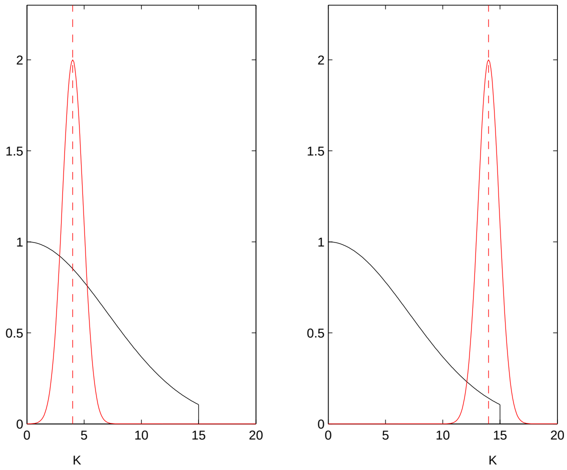

Figure 4.21: Schematic demonstration of the convolution of the electron-positron plane-wave coefficients a^{ep} according to eq. 3.5. The black curves represent the electron plane-waves, the red ones mean the positron plane-waves. Left: correct convolution for a small K; right: erroneous convolution for a large K [20].

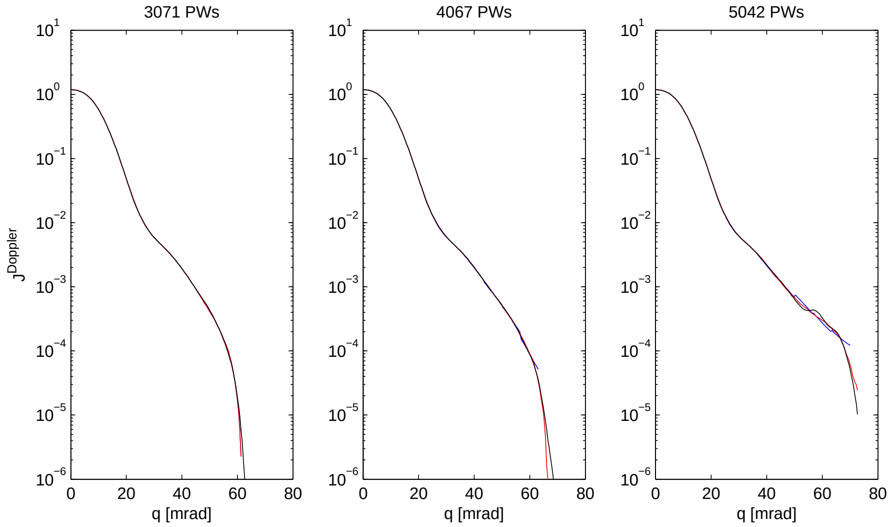

Figure 4.22: One-dimensional Doppler profiles for $Fe_{25}Cu_{75}$ (3s+3p) along the directions [100], [110] and [111], according to the IPM (without any enhancement), calculated by using different numbers of electron-positron plane-wave coefficients from a number of 6859 electron plane-wave coefficients.

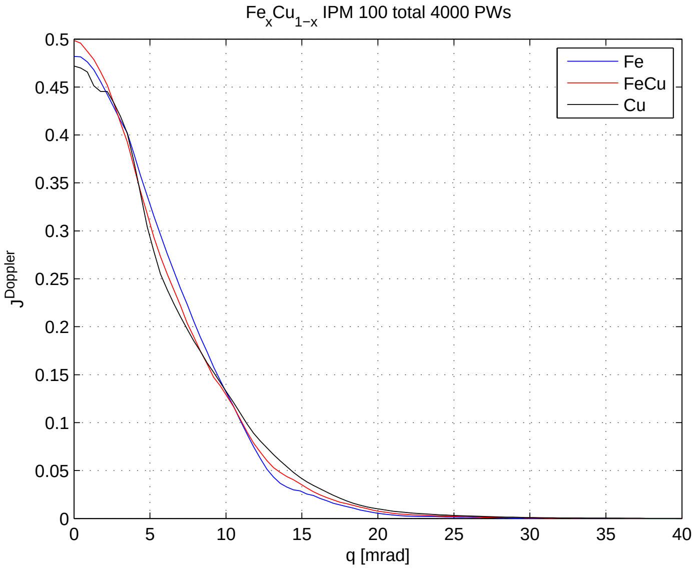

Figure 4.23: One-dimensional Doppler profile for Fe_xCu_{1-x} alloys along the [100]-direction according to the independent particle model (without any enhancement). All curves are normalized to the same area.

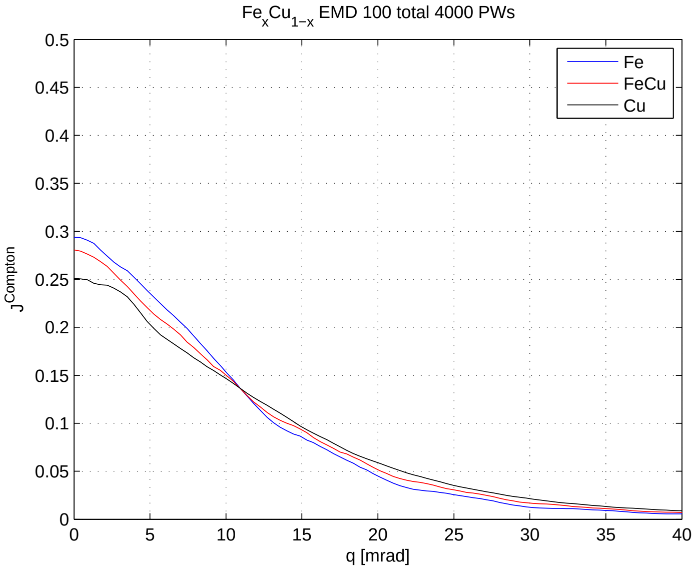

Figure 4.24: One-dimensional Compton profile for Fe_xCu_{1-x} alloys along the [100]-direction. All curves are normalized to the same area.

In fig. 4.23 the Doppler profiles (without any enhancement) for $\mathrm{Fe}_x\mathrm{Cu}_{1-x}$ alloys (for x=0, 0.5 and 1) are shown. Compared to the corresponding Compton profiles in fig. 4.24, the Gaussian shape is much sharper, hence, it is obvious that the annihilation rate takes highest values at small momenta. For higher momenta, the one-dimensional Doppler profiles take on rather small values, the annihilation rate almost vanishes in the high-momentum region. Further the Doppler profiles for Fe and Cu do not differ that much as the Compton profiles do, hence the effect of the Fe 3d electrons in the high-momentum region as described in sec. 4.1.1 does not occur any more.

Enhanced Doppler profiles: A measure to determine the practicability of the different parametrized enhancement factors (eqs. 3.12-3.14) and further, the reliability of the calculated Doppler profile, is the positron bulk lifetime as given in equation 2.10. Therefore, the Doppler profiles for copper using all enhancement factors given in section 3.2 have been calculated. The corresponding positron lifetimes are obtained by integration of the one-dimensional Doppler profiles (the bulk lifetime equals the reciprocal value of the area under the Doppler profile, see eq. 2.10). The results are shown in figure 4.25 and again in the semilogarithmic diagram fig. 4.26. Regarding the curves in 4.25 it turns out that the enhancement factors suggested by Boronski et. al. [19] and Puska et. al. [22] yield quite similar results throughout the whole region, while the curve calculated using the enhancement factor proposed by Barbiellini et. al. [23] yields significantly higher values and, hence, higher annihilation rates, especially for low momenta ($q < 15$ mrad). In the high-momentum region ($q > 35$ mrad), however, the three different enhancement factors yield quite similar results (fig. 4.26), hence, for an analysis of the Doppler profiles in this region, the choice of the enhancement factor only plays a minor role.

Positron lifetime experiments performed on copper turned out a bulk lifetime between 110 ps and 112 ps (Refs. [28],[29]). Hence, the formulas proposed in Refs. [19] and [22] yield quite good results in case of pure Cu, while the enhancement factor proposed in Ref. [23] does not seem to be applicable in this case. Therefore, all the following Doppler profiles presented in this chapter have been produced using formula 3.12.

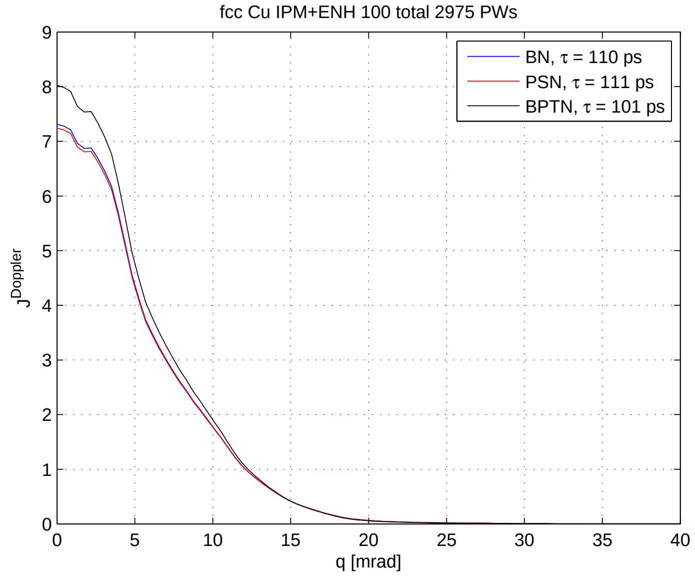

Figure 4.25: One-dimensional Doppler profiles for Cu along the [100]-direction using the different enhancement factors given in sec. 3.2 (BN=eq. 3.12, PSN=eq. 3.13, BPTN=eq. 3.14). τ means the bulk lifetime according to eq. 2.10.

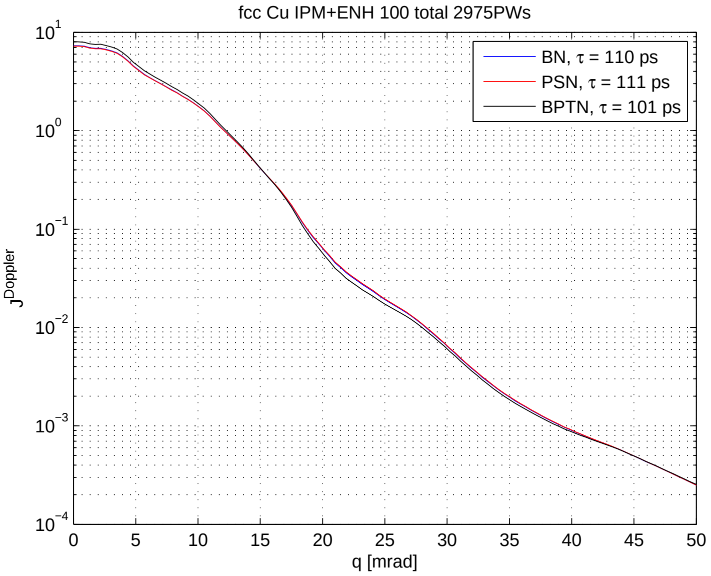

Figure 4.26: One-dimensional Doppler profiles for Cu along the [100]-direction using the different enhancement factors given in sec. 3.2 (BN=eq. 3.12, PSN=eq. 3.13, BPTN=eq. 3.14). τ means the bulk lifetime according to eq. 2.10.

A comparison of the one-dimensional Compton profile and the Doppler profiles using the independent particle model as well as the enhanced positron ground state for pure copper is shown in fig. 4.27. Again, the enhancement factor suggested by Boronski and Nieminen (eq. 3.12) has been chosen. Obviosly the contribution to the high-momentum region decreases by several orders of magnitude (note that this is a semilogarithmic diagram) when the positron ground state is taken into account. Hence, the overlap of the electron wave function and the positron ground state wave function decreases as q grows. At lower momenta, however, the enhanced Doppler profile assumes even higher values than the Compton profile. For a more detailed discussion of this effects, the contribution of the different electron bands to the total Doppler profile is shown in figure 4.28.

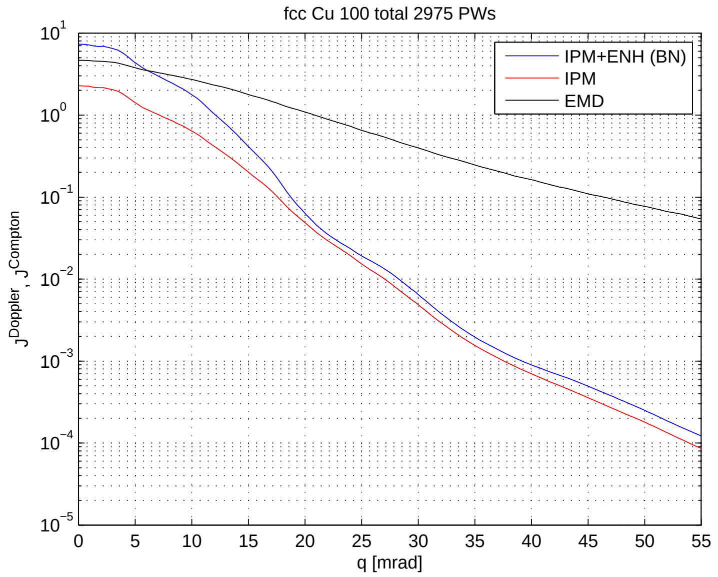

Figure 4.27: One-dimensional Compton and Doppler profiles for Cu along the [100]-direction.

Regarding the contributions of the different electron bands to the total Doppler profile (figs. 4.28 and 4.29) compared to their contributions to the Compton profiles (fig. 4.30), it turns out that the contribution of the valence states, that dominate the Compton profile up to a high-momentum region, is strongly decreased in case of the Doppler profile for higher momenta. For low momenta (up to 25 mrad), however, the contribution of the semi-core states is negligible and the profile in this region is almost completely determined by the valence states. Hence, the overlap of the positron wave function and the valence states wave function, that dominates the profile in the low momentum region, almost vanishes for higher momenta. On the other hand, the contribution of the semicore states, especially of the 3p bands, dominates the Doppler profile in the region of $q > 35$ mrad. Thus, according to figs. 4.28-4.30, a positron is most likely to annhihilate with an electron being in a valence state and having a small momentum, the overlap of the electron wave function and the positron wave function and, thus, the annihilation rate, takes on the largest values in this case. The rate decreases for higher momenta, but for annihilation processes taking place in the high-momentum region ($q > 35$ mrad), the electrons of the 3p bands play a major role.

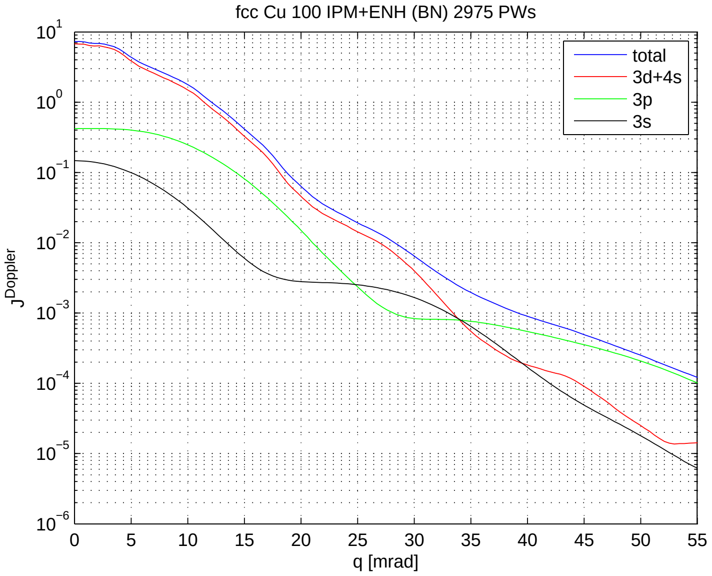

Figure 4.28: One-dimensional Doppler profiles for Cu along the [100]-direction using the enhancement factor suggested in Ref. [19] (eq. 3.12).

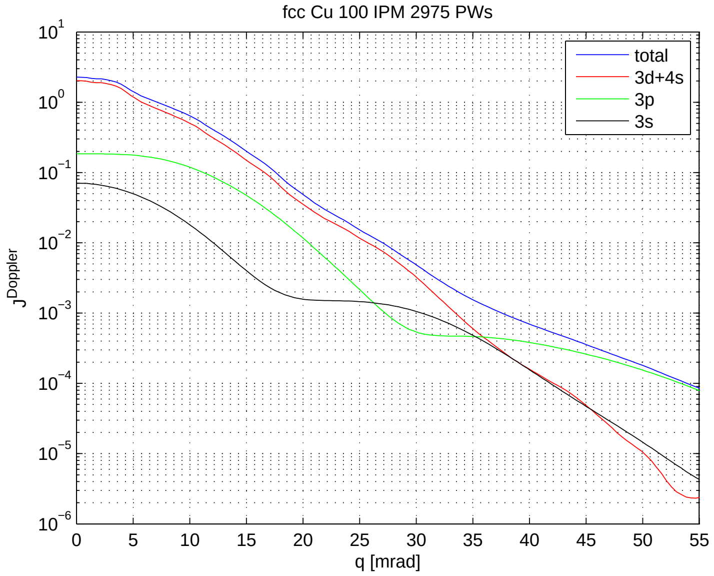

Figure 4.29: One-dimensional Doppler profiles for Cu along the [100]-direction according to the IPM.

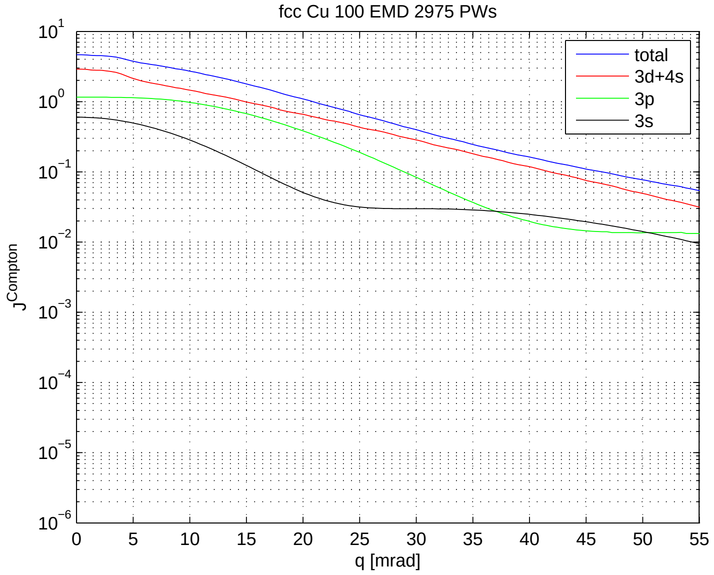

Figure 4.30: One-dimensional Compton profiles for Cu along the [100]-direction.

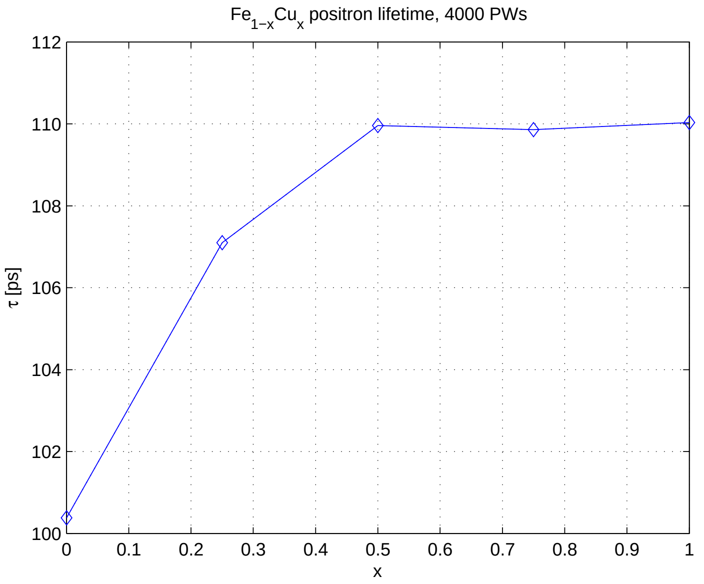

Figure 4.31: Dependence of positron lifetime τ in Fe$_{1-x}$Cu$_x$ alloys to the fraction of Cu x, determined according to eq. 2.10, using the enhancement factor suggested in Ref. [19] (eq. 3.12).

In fig. 4.31 the relation between the positron bulk lifetime τ and the fraction of Cu is shown. A comparison of the positron bulk lifetimes for pure Fe and Cu, calculated in this work, with theoretical results obtained by Campillo Robles et. al. [30], using the linear orbital muffin-tin method (LMTO) and the enhancement factor proposed by Boronski and Nieminen [19], and some experimental data is given in the following table:

Table 4.6: Some theoretical and experimental positron bulk lifetimes in bcc Fe and fcc Cu.

	τ_{Fe} [ps]	τ_{Cu} [ps]
theory:		
this work (LAPW-BN)	100	110
Campillo Robles et. al. [30] (LMTO-BN)	101	105
experiment:		
cited by Campillo Robles et. al.	111	120
cited by Barbiellini et. al. (1991) [31]	106	110
cited by Barbiellini et. al. (1995) [23]	112	120

As one can see in the table above, the values for the positron bulk lifetimes for pure Fe and Cu obtained in this work correspond quite well to other theoretical values in literature (see table 4.6), experimental data are somewhat higher than the calculated ones. A comparison of theoretical lifetimes with experimental ones, however, is difficult due to strong differences between the results of various experiments.

Further, one would assume the relation between the positron lifetime and the copper concentration to be linear, which is by far not the case in fig. 4.31. This might be due to two reasons

- a linear relation between lifetime and concentration will only exist if the relation between the concentration and the volume per atom is linear, which is not the case in the calculations performed in this work (values for the lattice constants can be found in table 4.4)
- another effect that might be the reason for this non-linear behaviour is called *preferential positron annihilation* (PPA) [32]: this means that there is a different affinity of the positron to the different partners of the alloy.

Regarding the figure above, the positron lifetime of pure Cu is obviously already reached at a fraction of Cu $x = 0.5$. This might be a sign that the second reason mentioned above (PPA) is the main effect yielding this non-linear behaviour. A possible explanation is that the positron's affinity to annihilate with an Cu electron is such higher than for annihilation with an Fe electron, that for $x = 0.5$ all positrons annihilate at Cu electrons having a lifetime close to the one in pure Cu. In order to distinguish between these two effects, however, more detailed theoretical investigations will be necessary.

5 Acknowledgments

I would like to express profound gratitude to my advisor Ao. Univ.-Prof. Dipl.-Ing. Dr. techn. Heinrich Sormann. Without his patience, supervision, advice and his invaluable support, this thesis would never have been completed. One simply could not wish for any better or friendlier supervisor.

Furthermore, I want to thank all people who accompanied me during my study.

Last, but not least, I would like to express my gratitude to my family and my friends for their support throughout my study.

Bibliography

[1] Positron Spectroscopy of Solids, edited by A. Dupasquier and A. P. Mills, IOS Press, Amsterdam (1995).

[2] M. Šob, H. Sormann and J. Kuriplach, Adv. Quant. Chemistry **42**, 77 (2003).

[3] A. Bansil, Z. Naturforsch. Teil A **48a**, 165 (1993).

[4] W. Schülke, G. Stutz, F. Wohlert and A. Kaprolat, Phys. Rev. B **54**, 14381 (1996).

[5] Positrons in Solids, edited by P. Hautojärvi, Springer-Verlag, Berlin, 1979.

[6] P. Blaha, K. Schwarz, G. K. H. Madsen, D. Kvasnicka and J. Luitz, *WIEN2k*, An Augmented Plane Wave + Local Orbital Program for Calculating Crystal Properties (Karlheinz Schwarz, Techn. Universität Wien, Austria), 2001. ISBN 3-9501031-1-2

[7] J. T. Wang, L. Zhou, Y. Kawazoe and D. S. Wang, Phys. Rev. B **60**, 3025 (1999).

[8] European Nuclear Society.
Internet: http://www.euronuclear.org/info/encyclopedia/comptoneffect.htm (accessed 12 October 2010)

[9] M. J. Cooper, Rep. Prog. Phys. **48**, 415 (1985).

[10] H. Sormann, Phys. Rev. B **54**, 4558 (1996).

[11] H. Sormann and G. Kontrym-Sznajd, Phys. Rev. B **73**, 075111 (2006).

[12] S. Daniuk, G. Kontrym-Sznajd, J. Mayers, A. Rubaszek, H. Stachowiak, P.A. Walters, and R.N. West, in *Positron Annihilation*, edited P.C. Jain, R.M. Singru, and K. P. Gopinathan (World Scientific, Singapore, 1985), pp. 43 and 279; S. Daniuk, G. Kontrym-Sznajd, A. Rubaszek, H. Stachowiak, J. Mayers, P.A. Walters, and R.N. West, J. Phys. F *17*, 1365 (1987); S. Daniuk, M. Šob, and A. Rubaszek, Phys. Rev. B **43**, 2580 (1991).

[13] H. Sormann, private communication (2010).

[14] P. E. Mijnarends, A. C. Kruseman, A. van Heen, H. Schut and A. Bansil, J. Phys.: Condens. Matter **10**, 10383 (1998).

[15] Z. Tang, M. Hasegawa, Y. Nagai, M. Saito and Y. Kawazoe, Phys. Rev. B **65**, 045108 (2002).

[16] M. Alatalo et. al., Phys. Rev. B **51**, 4176 (1995)

[17] P. Hohenberg and W. Kohn, Phys. Rev. B **136**, B864 (1964).

[18] W. Kohn and L. J. Sham, Phys. Rev. **140**, A1133 (1965).

[19] E. Boronski and R. M. Nieminen, Phys. Rev. B **34**, 3820 (1986).

[20] H. Sormann, *Theoretical treatment of Doppler broadening experiments* (2009).

[21] J. Arponen and E. Pajanne, Ann. Phys. (NY) **121**, 343 (1979).

[22] M. J. Puska, A. P. Seitsonen and R. M. Nieminen, Phys. Rev. **52**, 10947 (1995).

[23] B. Barbiellini, M. J. Puska, T. Torsti and R. M. Nieminen, Phys. Rev. B **51**, 7341 (1995).

[24] D. J. Singh and L. Nordström, *Planewaves, Pseudopotentials, and the LAPW Method* (Springer Verlag, 2006).

[25] TETPACK Library.
Internet: http://www.fundp.ac.be/sciences/physique/administration/tetpack/setk.html

[26] P. A. Serena and N. Garcia, Phys. Rev. B **50**, 944 (1994).

[27] Crystal Lattice Structures.
Internet: http://cst-www.nrl.navy.mil/lattice/spcgrp/index.html (accessed 31 May 2010)

[28] H. E. Schaefer, W. Stuck, F. Banhart and W. Bauer, *Proceedings of the International Conference on Vacancies and Interstitials in Metals and Alloys*, edited by C. Ambromit and H. Wollenberger (Trans Tech, Aedermannsdorf, Switzerland, 1986).

[29] K. O. Jensen, M. Eldrup, S. Linderoth and J. H. Evans, *Proceedings of the 8th International Conference on Positron Annihilation*, edited by L. Dorikens-Vanpraet, M. Dorikens and D. Segers (World Scientific, Singapore, 1988).

[30] J. M. Campillo Robles, E. Ogando and F. Plazaola, J. Phys.: Condens. Matter **19**, 176222 (2007).

[31] B. Barbiellini, P. Genoud and T. Jarlborg, J. Phys.: Condens. Matter **3**, 7631 (1991).

[32] J. Dryzek, Phys. Status Solidi B **246**, 2238 (2009).